NEUTRONIC, THERMAL HYDRAULIC, AND SYSTEM DESIGN SPACE ANALYSIS OF A LOW ENRICHED NUCLEAR THERMAL PROPULSION ENGINE

A Thesis
Presented to
The Academic Faculty

by

Matthew Andrew Krecicki

In Partial Fulfillment
of the Requirements for the Degree
Masters of Science in
Nuclear and Radiological Engineering

Georgia Institute of Technology
December 2019

NUETRONIC, THERMAL HYDRAULIC, AND SYSTEM DESIGN SPACE ANALYSIS OF AN LOW ENRICHED NUCLEAR THERMAL PROPULSION ENGINE

Approved by:

Dr. Dan Kotlyar, Advisor
School of Mechanical Engineering
Georgia Institute of Technology

Dr. Jonathan Witter
Chief Engineer
BWX Technologies

Dr. Nolan E. Hertel
School of Mechanical Engineering
Georgia Institute of Technology

Date Approved: November 15, 2019

I would like to dedicate this thesis to my family, friends, lab-mates, team-mates, and colleagues that made my time at Georgia Tech a truly remarkable experience.

ACKNOWLEDGEMENTS

This work was funded through the Nuclear Regulatory Commission NRC Fellowship 3130018M0020. The author would also like to thank Dr. Jonathan Witter for his advice and expertise on nuclear thermal propulsion design.

TABLE OF CONTENTS

LIST OF TABLES

LIST OF FIGURES

LIST OF SYMBOLS AND ABBREVIATIONS

2D	Two-Dimensional
3D	Three-Dimensional
ANL	Argonne National Laboratory
BATH	Boron Carbide Titanium Hydride
Be	Beryllium
BeO	Beryllium Oxide
FE	Fuel Element
I_{sp}	Specific Impulse
LEU	Low Enriched Uranium
LWR	Light Water Reactor
MC	Monte Carlo
ME	Moderator Element
Mo	Molybdenum
MWt	Mega-Watt Thermal
NASA	National Aeronautical and Space Administration
NERVA	Nuclear Engine for Rocket Vehicle Applications
NTP	Nuclear Thermal Propulsion
PWR	Pressurized Water Reactor
T/H	Thermal Hydraulic
U-235	Uranium 235
UN	Uranium Nitride
UO_2	Uranium Dioxide
W	Tungsten
ZrC	Zirconium Carbide
ZrHx	Zirconium Hydride

SUMMARY

Nuclear thermal propulsion is the high thrust, high specific impulse rocket engine technology of choice for future missions to Mars and beyond. Chemical rocket engines have a maximum specific impulse of approximately 450 seconds. A nuclear engine achieves considerably higher specific impulse of ~ 900 seconds due to its high power density. The factor that limits the specific value from being even higher is the thermal constraints of the material components (e.g. melting temperature).

Legacy designs studied during the ROVER/NERVA program demonstrated the feasibility of different material compositions, various core configurations and hence engines to achieve a specific impulse. However, the fuel relied on highly enriched uranium of above 90%.

Current designs are focusing on low enriched uranium fuel systems to reduce development costs, regulatory concerns and deploy this technology promptly. These designs require careful examination to identify an engine that is able to satisfy NASA's requirements. Recent work did focus on low enriched fuel, but only limited fuel options were studied for the engine design. Moreover, the complex nature of nuclear thermal propulsion systems require computational framework capable to model the fully integrated system (e.g. core, turbine, pumps, etc.). However, typically the computational approach decouples the various components while adopting the assumption that the boundary conditions to each individual component (e.g. core) are known and fixed. This results in a non-conservative approach, which this thesis attempts to overcome. The main focus is to

develop an integrated neutronic, thermal hydraulic, and system computational sequence to enable a conservative search for an optimum design.

All the information adopted here to study various designs has been collected from publicly available sources.

This thesis relies and extends on previously published NASA studies by accounting for UN fuel embedded in Mo and Mo-W matrices to form an axially split core. Integrated system analyses are developed to account for neutronic, thermal hydraulic, and system effects on engine performance. The results show that using an integrated system analyses approach yields a systematic assessment and identifies an ideal design space for future higher fidelity analysis to achieve mission needs set by NASA.

CHAPTER 1. INTRODUCTION

This chapter presents historical designs, the adopted methodology, and numerous analyses related to study the performance of a nuclear thermal propulsion engine. The following sections will lay out the motivation for the work, the objectives of the thesis, and a description of the work performed.

1.1 Motivation

Nuclear thermal propulsion (NTP) systems have been selected by NASA for Mars and deep space missions. NTP systems have a significant advantage over chemical and electrical systems, due to their high specific impulse (I_{sp}) and high thrust. Chemical rocket engines have a maximum specific impulse of approximately 450 seconds, while NTP's can achieve I_{sp}'s of 900 seconds or even higher. Electrical propulsion systems yield I_{sp}'s of 3000 seconds but suffer from extremely low thrust values, on the order of a few pounds of thrust produced. Typical thrust values for nuclear rockets are 10-100 klb_f [1]. These performance parameters yield numerous benefits for inter-planetary travel. NTP's can enable mission abort modes not possible with other propulsion architectures [2]. Additionally, NTP's can significantly reduce Mars transit times which results in a decrease in astronauts' cosmic ray exposure. Currently, NTP designs are limited to the use of low enriched uranium (LEU), which places significant limitations on the design space and requires detailed analysis.

1.2 Objectives

The main objective of the thesis is to determine an ideal design space for LEU NTP systems, and identify key parameters for further higher fidelity analysis. This is accomplished by:

- Developing a neutronic model in Serpent to study various core configurations. This also includes developing an automatic Serpent input generator to efficiently generate and study thousands of different core configurations.
- Developing a method to accurately model the thermal hydraulic phenomena present in the engine. More specifically, the method should have the ability to model the counter flow of the hydrogen propellant in the system and evaluate the spatial heat transfer accurately.
- Developing a method to accurately calculate the boundary conditions of an NTP expander cycle. This allows to model the integrated system simultaneously rather than assuming some groundless and fixed boundary conditions.

1.3 Scope

As a starting point, the first portion of the work relates to developing the computation codes to model numerous reactor cores models with various moderator to fuel element ratios, and axial split ratios. This capability will allow for a unique neutronic solution for each case in the design space. The NERVA KIWI-4BE element geometry was chosen as the reference design for this thesis. All Monte Carlo simulations presented in this work were performed using Serpent, with coupled neutron and gamma transport. This allows for photon heating effects to be accounted for. The second section of the work

relates to the development of an NTP system and thermal hydraulic code used to calculate engine performance. Nuclear thermal propulsion engines have several unique features not found in other reactor types, such as counter flow inside the moderator elements, and heat transfer from the fuel elements to the moderator elements. These characteristics should be accounted for to provide accurate thermal hydraulic solutions. Additionally, the boundary conditions for each flow channel are dependent upon the engine system feedbacks, which are accounted for in the system code. The final section of work relates to the design space analysis for various perturbations made to the design. This task involves the calculation of numerous cases to fully probe the design space. Once all analysis was completed a final region of interest was defined for future higher fidelity analysis.

1.4 Thesis Layout

Chapter 2 presents valuable background information, which is critical to the current work, including descriptions of the historical NTP designs, modern NTP designs, and current NASA performance requirements. All information pertaining to modern nuclear thermal propulsion designs has been obtained from publicly available sources and previously published research. Chapter 3 provides a detailed description of the core configuration and materials used. The codes and computational methods adopted, developed and implemented in this these are described in Chapter 4. Extensive sensitivity studies were carried here and are presented in Chapter 5. Chapter 6 contains the bulk of the work, where the design space is generated, followed by extensive neutronic and T/H

analyses. This chapter also identifies an ideal design space for future investigations. Finally, Chapter 7 contains the conclusions and future work statements.

CHAPTER 2. BACKGROUND

In this chapter, an overview of historical and modern nuclear thermal propulsion engine designs is given. In addition, current NASA design requirements are explained. Information from this chapter will be used as a baseline throughout the entire thesis.

2.1 Introduction

Nuclear thermal propulsion (NTP) systems have been selected by NASA for Mars and deep space missions. Nuclear thermal propulsion is not a 21st century concept, and the technology was extensively developed in the 1960's through the 1970's. The Nuclear Engine for Rocket Vehicle Application (NERVA) program was the largest NTP design development effort ever conducted. The program generated a large library of invaluable technical reports and experimental data. Over 20 different reactor concepts were designed, built, and tested. Another less well known NTP design effort was conducted by Argonne National Lab (ANL) in the 1966 which yielded two designs, the ANL-2000 and the ANL-200. This program was a concept design study only, and included a fuel development program; however no engines were ever constructed following this program [3]. Despite the significant amount of progress made by the NERVA program, there is still a large amount of research and development required to achieve NASA's future goals. Recent development programs have focused on LEU fuel systems to reduce development costs and regulatory concerns. The work in this thesis focuses on the advancement of LEU engine designs. It is worth stating the NTP design efforts lay down the ground work for other advanced reactor concepts. Many of the designs and fuel materials developed in NTP programs have direct applications to higher temperature systems and micro reactors.

2.2 NERVA

The NERVA program was an effort by NASA and the Atomic Energy Commission (AEC) to mature nuclear thermal propulsion technology. The main objectives of the program were to design, build, and test engines to assess the real performance and operation characteristics of NTP's. To achieve these goals multiple test fires were performed at Jackass Flats, Nevada. A summary of test concepts and their initial test date and reactor power is presented in Table 2.1.

Table 2.1 Summary of NERVA Test Engines [4]

Engine	**Test Date**	**Reactor Power [MWt]**
KIWI-A	July 1, 1959	70
KIWI-A3	October 10, 1960	100
KIWI-B1A	December 7, 1961	300
KIWI-B1B	September 1, 1962	900
KIWI-B4A	November 30, 1962	500
KIWI-B4D	May 13, 1964	1000
KIWI-B4E	July 28, 1964	900
NRX-A2	September 10, 1964	1100
NRX-A3	April 23, 1965	1165
PHOEBUS-1A	June 25, 1965	1090
NRX-EST	March 2, 1966	1100
NRX-A5	June 23, 1966	1140
PHOEBUS 1B	February 23, 1967	1500
NRX-A6	December 13, 1967	1100
PHOEBUS-2A	June 26, 1968	4000
PEWEE	December 3, 1968	514
XE-PRIME	June 11, 1969	1100

2.2.1 KIWI

The KIWI series consisted of eight ground test reactors from mid-1959 to mid-1964. Each design iteration implemented design changes from the previous designs to enhance engine operational performance and reliability. The KIWI-A reactor utilized a central D_2O moderator island, surrounded by four layers of high enriched uranium UO_2 plate fuel. The outer core diameter was 33 inches and a height of 54 inches. [5] The results of the KIWI-A testing revealed that some of the fuel element temperatures in excess of 2900 degrees kelvin; similar centerline temperatures are expected in modern nuclear thermal propulsion engines. These extreme centerline temperatures resulted in several fuel element failures where some fuel fragments were ejected from the nozzle. The KIWI-A3 design moved from plate-type fuel to cylindrical type, having 4-hole cooled graphite fuel elements. Figure 2.1presents the KIWI-A3 fuel element design. Similar to the previous design, KIWI-A3 suffered from fuel structural damage, which suggested that the tensile loads on graphite structures should be avoided.

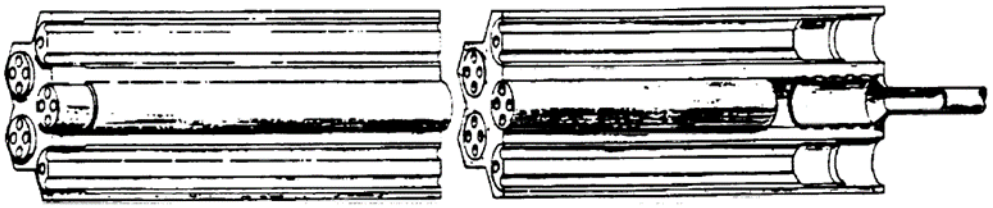

Figure 2.1 KIWI-A3 Fuel Element Design [6]

The KIWI-B test series was designed to achieve a reactor power of 1000 MWt. One of the most significant design changes from the KIWI-A series was the removal of the central moderating island, and the implementation of control drums. The control drums were

cylindrical drums composed of the reflector material and partially lined with a neutron poison, typically boron carbide. Rotating the poison surface towards the core reduces reactivity and rotating the poison surface away increases it. This control system been adopted into almost every modern NTP design, and several micro reactor concepts. The control drums were placed inside a beryllium radial reflector. The fuel element design was modified to increase the number of coolant channels from four to seven; this reduced the fuel element web thickness and resulted in lower thermal gradients inside the fuel element. The final engine design is presented in Figure 2.2.

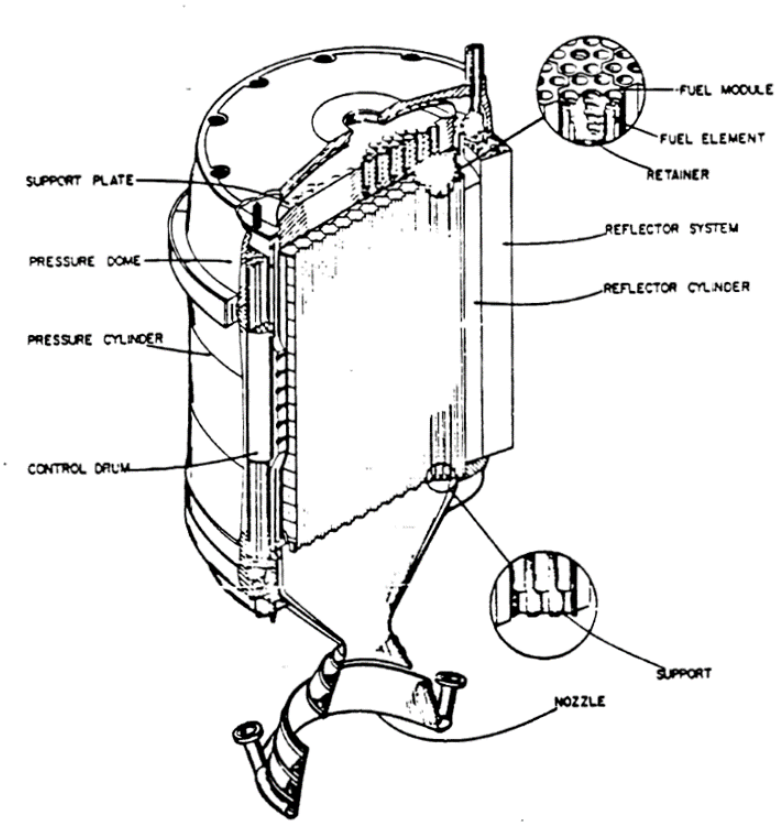

Figure 2.2 KIWI-B1B Engine Design [6]

The KIWI-B1B design did not perform as expected during testing. Nozzle flashing was observed at full power, which indicated that fragments of the fuel were exiting through the nozzle, and test was terminated after a few seconds at full power. Post-test inspection revealed that 50 fuel elements were severally damaged. In order to determine the cause of the fuel element damage in the KIWI-B series reactors cold flow testing was conducted on the KIWI-B4A design. These tests were performed on fuel elements without any uranium loaded, and therefore produced no power. The tests were performed with gaseous nitrogen, helium, and hydrogen. The tests demonstrated that structural core damage was due to flow-induced vibrations. These effects were present when the exit Mach number of the exiting flow approached 0.3 [6]. This Mach number limitation has been used as an engineering limit in the current thesis, which places restrictions on the velocity, pressure drop and mass flow rate across the core.

The final reactor in the KIWI series was KIWI-B4E. This design implemented all of the design lessons from the previous KIWI experiments. The test of this design was described as "smooth and uneventful" [6]. The KIWI test reactor series provided a technically sound baseline design for the NERVA program to expand to larger higher thrust designs.

2.2.2 PHOEBUS

The Phoebus test series had the highest reactor power and thrust among all the NTP designs in the NERVA program. The thermal power output of Phoebus-2A was 4000 MWt, which is comparable and even greater than a typical light water reactor power output.

However, due to the considerably more compact NTP dimensions, the power density was considerably higher.

The Phoebus design utilized fuel elements with a height of 132 centimeteres, and a flat-to-flat distance of 1.91 centimeteres, and contained 19 coolant channels. The coolant channels were cladded with niobium carbide (NbC) and over-coated with molybdenum (Mo). The reason for the Mo overcoat was to address the midrange corrosion problem. The central third of the fuel element flow channels observed the highest degree of corrosion due to the highest power density occurring in the center of the reactor. The NbC coating experienced severe cracking in the midrange due to the mismatch of the thermal expansion coefficient and increased thermal gradients. The Mo overcoat reduced the corrosion effects and reduced the fuel mass loss during testing. The results of the Phoebus testing showed excellent mechanical and thermal performance. The successful Phoebus test series was a milestone in nuclear thermal propulsion technology and was particularly notable as the highest power gas cooled reactor ever operated. At the conclusion of the test series, the Los Alamos National Lab (LANL) team recommended that further work should focus on the study of the neutronics of NTP's [6].

2.2.3 PEWEE

The purpose of the PEWEE test series was to accelerate the advancement of fuel element designs. The basic design was similar to the Phoebus engine but contained several unique design changes. The active core diameter was reduced to 53.34 centimeters to reduce the number of fuel elements in the core. In order to compensate for the loss of reactivity, a zirconium hydride (ZrHx) sleeve were integrated into the tie-tubes. This design

change marks the transition from tie-tubes to moderator elements (ME). The hydrogen rich ZrHx provided moderation and reduced the minimum critical mass of uranium for the system. The use of moderator elements is a key design feature of all modern low enriched NTP designs. The effective use of moderator elements will also be a key design parameter in this thesis. An example of a typical Pewee fuel element and moderator element cluster is presented in Figure 2.3. The moderator element serves two purposes in modern nuclear thermal propulsion designs, structural support, and moderation. The moderator elements are affixed to the upper support plate and provide support to the surrounding fuel elements. This isolates the fuel elements from any tensile stress, which the KIWI test series provided to be vital for engine reliability. The Pewee fuel and moderator element pattern has been used extensively in historical and contemporary NTP designs, additionally the inverse Pewee pattern is where a single fuel element has six surrounding moderator elements. This configuration is more common in LEU NTP designs due to the increased moderation.

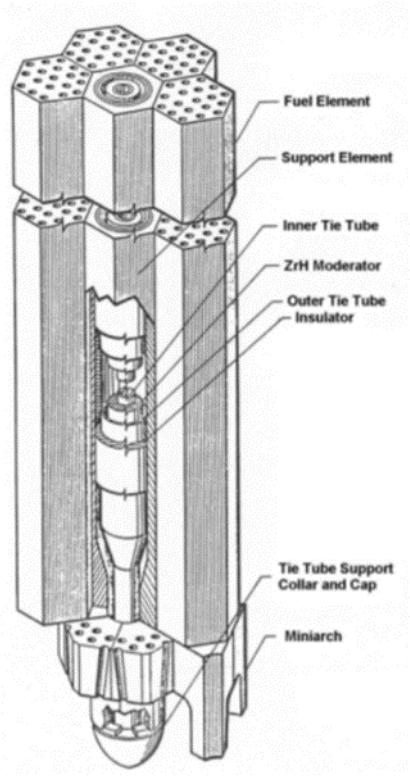

Figure 2.3 Pewee Fuel and Moderator Element Cluster [6]

2.3 ANL-200/2000

The studies conducted by Argonne National Lab (ANL) in 1966 yielded two designs, the ANL-2000 and the ANL-200. The ANL-2000 was a 2000 MW_t engine, which produced 110 klb_f of thrust with an I_{sp} of 832 seconds. The ANL-200 was a 200 MW_t engine that produced 10.5 klb_f of thrust with an I_{sp} of 821 seconds. One of the unique features of the ANL-200 design was its two-zone fuel element design. The upper half (*i.e.*, closer to the coolant inlet) of the core that experiences lower fuel temperatures uses a molybdenum-urania matrix, while the lower half (*i.e.*, closer to the nozzle) of the core uses a tungsten-molybdenum-urania matrix due to the elevated temperatures. (ANL, 1966).

Most of the research and development problems which were considered in the design effort focused on a similar fuel element design.

2.3.1 ANL-2000

The ANL-2000 design was similar to the NERVA reactors, in the fact that it utilized a beryllium reflector, and control drums to control core reactivity. However, the active core region utilized a refractory ceramic metallic (cermet) fuel. The active core region also lacked moderator elements which allowed the core to maintain a fast neutron spectrum. However, the active core was surrounded by preheater assemblies. This configuration is presented in Figure 2.4. The preheaters provided the energy required to power the turbo-machinery.

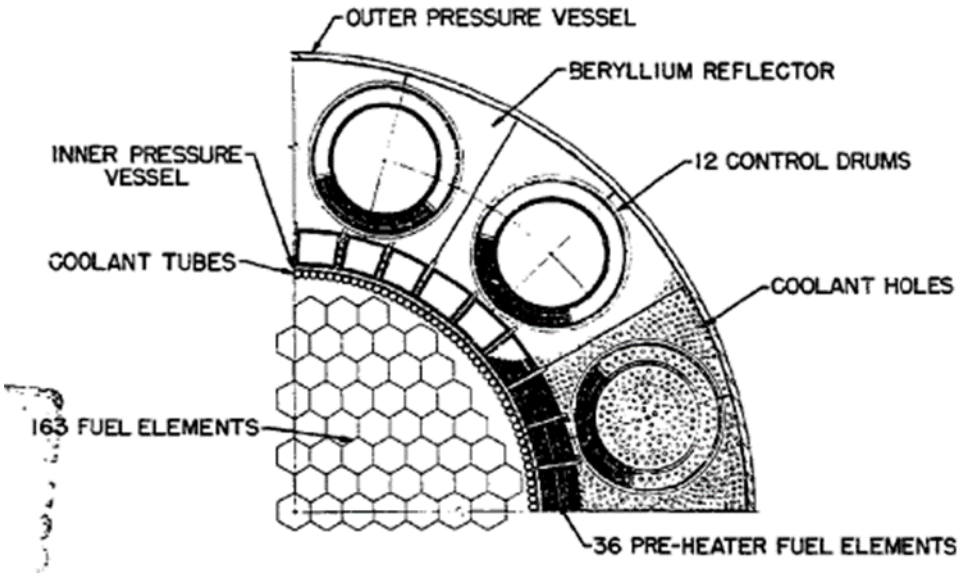

Figure 2.4 ANL-2000 Core Cross Section [3]

The fuel elements in the ANL-2000 design loaded 93% enriched uranium into a tungsten-based cermet fuel, with a 60-volume percent packing of fuel.

2.3.2 ANL-200

The ANL-200 design differed in two major ways from the ANL-2000 design. The first is the implementation of a two-zone fuel element, and the second is the method of reactor control. A comparison of the scale of the two systems is shown in Figure 2.5. The ANL-200 design is more representative of current NTP designs which focus on compactness, and thrust to weight ratio.

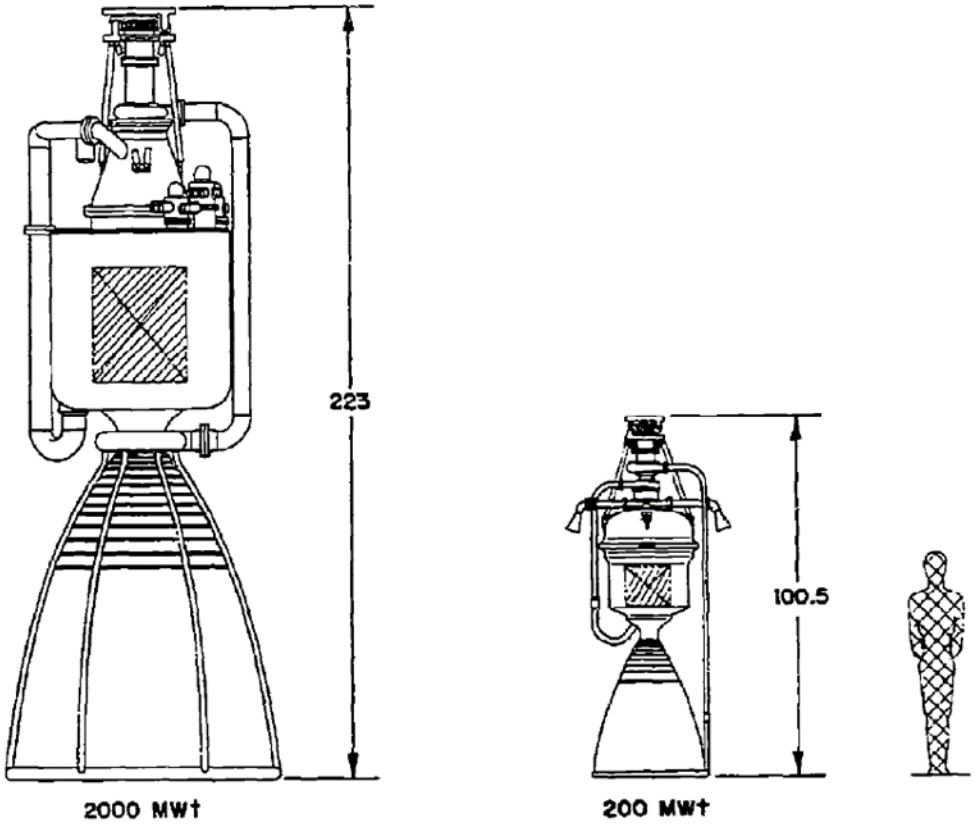

Figure 2.5 Comparison of ANL-2000 and ANL-200 Engine [3]

The ANL-200 design managed excess reactivity through the use of a movable radial reflector, which increased or decreased the neutron leakage rate. The two-zoned fuel element concept takes advantage of molybdenum physical properties to reduce the total system weight. The molybdenum-Urania matrix is used in place of the tungsten-urania matrix is the upper half of the core where the gas and centerline fuel temperatures are reduced. Figure 2.6 shows the axial configuration of the ANL-200 design, where the fuel sections represent the two-zone fuel elements. The axial split of the ANL-200 was fixed with half of the core using a Mo cermet, and the lower half using a W cermet. Varying this ratio will be a key design parameter in this thesis.

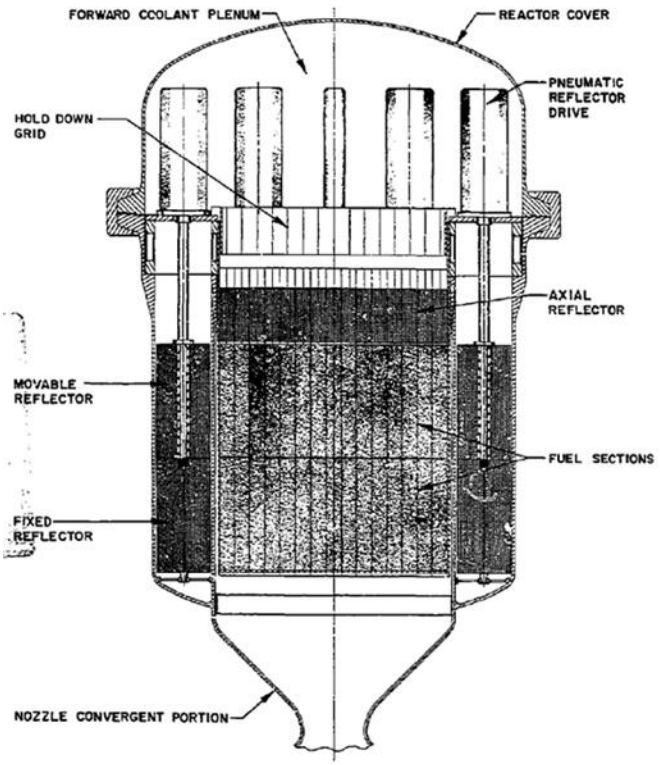

Figure 2.6 ANL-200 Axial Configuration [3]

2.4 Modern Designs

All information pertaining to modern nuclear thermal propulsion designs has been obtained from publicly available sources. Despite the significant amount of progress made by the NERVA program there is still a large amount of research and development required to achieve NASA's future goals. The largest shift in design philosophy from historical to current NTP designs is the requirement of a low-enriched uranium (LEU) fuel systems [7]. The use of LEU significantly decreases the regulatory concerns [8], which the NERVA program was not subjected to. All of the previous NERVA and ANL designs relied on HEU based fuel that allowed to minimize the active core dimensions and resulted in a relatively flat power distribution. Current NTP designs have taken aspects from each of the previous development programs, such as an axial split fuel system, use of moderator elements, radial beryllium reflectors, and control drums to provide a compact high-performance engine, while relying on a LEU based fuel system. One of the largest challenges of current NTP designs is maintaining enough excess core reactivity while satisfying the thermal-hydraulic limits. This challenge arises since the LEU design mandates some form of moderation, which is typically achieved by incorporating moderating elements. However, the moderation also means that tungsten isotopes, most of which have high absorption cross-sections, introduce a large reactivity penalty.

Previous work has utilized a refractory ceramic metallic fuel (cermet) with enriched tungsten to limit and reduce the parasitic neutron absorption [9]. In order to maintain a critical system tungsten must be highly enriched to contain almost entirely W^{184}. However, obtaining enriched tungsten can require extremely long lead times and have extreme manufacturing costs [10]. One of the most recent updates from NASA's NTP game

changing development (GCD) program [11] have stated that NTP's will only be utilized if the development is affordable and viable. In order to improve the viability of the system an axially split system is envisioned in our design. Similar to the ANL designs, the cooler regions of the engine (<2000 K) use a Mo/UN ceramic metallic alloy, while the hotter regions (>2000 K) use a Mo/W dispersion strengthened metal alloy in conjunction with UN or UO_2 fuel [13]. Additional, updates have placed a strong focus on the use of a "graded Mo to Mo/W" fuel system, similar to the ANL-200 design [12][13][14].

2.5 NASA DRA-5.0 Requirements

The primary design requirements document for our study is NASA's Mars Design Reference Architecture (DRA) 5.0 [15]. In this document and its addenda NASA defines all aspects of a possible Mars exploration campaign. The two major propulsion systems considered in the DRA are nuclear thermal propulsion and advanced thermal propulsion with aerocapture at Mars. Nuclear thermal propulsion is the preferred option due to the significantly lower propellant mass requirements and increased mission flexibility.

The major assumptions made about NTP system performance act as the baseline requirements in this thesis. The major design requirements relate to the specific impulse, thrust, and thrust-to-weight ratio. The assumed specific impulse in the DRA 5.0 is between 875 and 900 seconds, however all calculations are performed with an I_{sp} of 900 s. Additionally, all mission profiles are calculated with a total thrust of 75 klb_f, relying on a cluster of three engines. Therefore, each engine should at least be able to produce 25 klb_f of thrust. The NTP core stage dry mass is assumed to be on the order of 33 metric tons, which corresponds to a thrust-to-weight ratio of 3.5. However, the total core weight should

be considered as a function to be minimized. These requirements are summarized in Table 2.2 A final constraint on the NTP system is the total volume of the propulsion stage. The engine cluster must be able to fit within a 10 meter diameter shroud, therefore a single engine may not have a diameter larger than 4.6 meters. NASA also recommends to pursue any design option that improve mission economics and trip times.

Table 2.2 NASA DRA 5.0 NTP Engine Performance Requirements [15]

Performance Requirement	**Unit**	**Value**
I_{sp}	s	875-900
Thrust	klb_f	25
Thrust to Weight Ratio	unitless	3.5
Engine Mass	lbs	7143
Engine Outer Diameter	m	4.6

CHAPTER 3. DESIGN DESCRIPTION

The work presented herein uses the KIWI-4BE fuel element design, and Pewee-1 moderator element design developed during the NERVA program. These core elements were tested during the NERVA program and were found to be mechanically and structurally acceptable. The geometry web thickness has been previously manufactured, and should not impose any major manufacturing limitations. The fuel system adopted here will focus on a similar fuel system proposed by NASA and detailed in section 2.4.

3.1 Core Elements

3.1.1 Fuel Element

As stated previously, the element geometry is based off of the KIWI-4BE design, which featured 19 coolant channels with a diameter of 0.3454 cm, cladding thickness of 150 micrometers, and a fuel element flat to flat of 1.905 cm. The fuel element dimensions are listed in Table 3.1, and displayed in Figure 3.1.

Table 3.1 Fuel Element Geometry Parameters [6]

	Unit	**Value**
Flat to Flat Distance	cm	1.905
Coolant Channel Radius	cm	0.1727
Cladding Thickness	cm	0.015

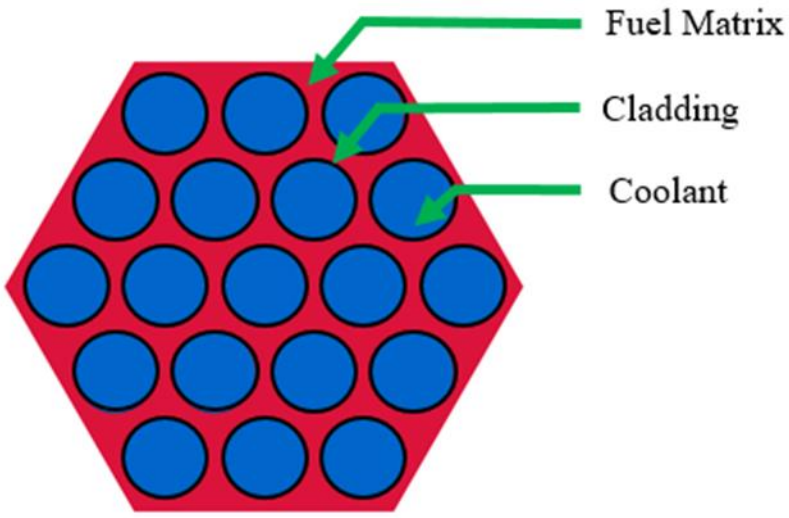

Figure 3.1 KIWI-B4E Fuel Element Geometry

The fuel type selected for the NTP core is a refractory ceramic metallic fuel. The advantage of cermet fuels is their extremely high melting temperature (3695 K), thermal conductivity (above 100 $\left[\frac{W}{m\,^{\circ}K}\right]$ for all operating temperatures [17]), compatibility with a hydrogen, and radiation environment. In addition, it exhibits the lowest vapor pressure of all group IV refractory metal metals [18]. The main disadvantage of cermet fuels is the high neutron absorption cross section associated with the refractory metal matrix material, which is dominated by the (n,γ) capture reaction. Previous work has relied on fuel composed of 19.75% enriched UO_2 particles embedded in a tungsten matrix with 6 mol% ThO_2 introduced as a stabilizer [16]. This thesis work extends the design work performed previously by adopting a two-split design similar to the one used in the ANL designs. The latter relied on tungsten and molybdenum uranium dioxide fuel embedded in the cermet fuel matrix [3]. Molybdenum is an attractive alternative due to its reduced neutron

absorption cross section and comparable thermal conductivity. Figure 3.2 compares the effective (n, γ) capture cross sections of natural molybdenum and natural tungsten. Figure 3.2 shows that utilizing molybdenum can greatly reduce the capture cross section of the fuel matrix material in the thermal energy range. Overall, this figure shows that molybdenum absorbs less neutrons when compared to tungsten, even in the epi-thermal and fast energy ranges.

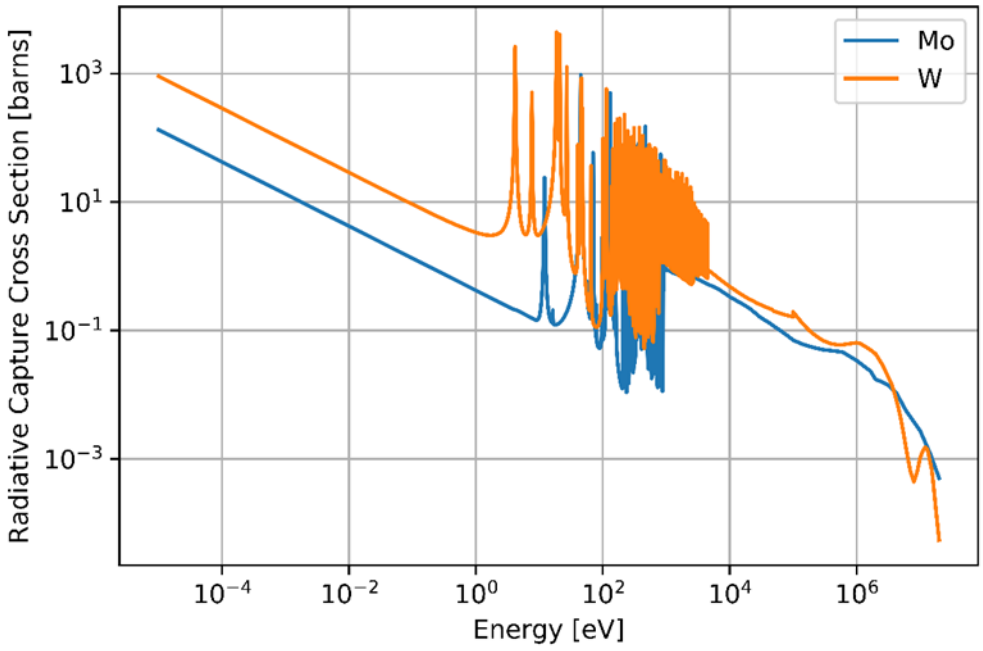

Figure 3.2 Tungsten and molybdenum capture cross section comparison. [19]

However, molybdenum has a much lower melting temperature of 2890 K, and an increased vapor pressure [20]. Therefore, molybdenum can only be exposed to relatively cold temperatures, and hence cannot be used to replace the tungsten matrix entirely.

The most common fuel kernel used in NTP cermets is UO_2, which was a sufficient choice in legacy HEU designs. However, the current LEU designs could benefit from an increased HM loading. A potential candidate with good thermal properties and increased HM loading fuel is the uranium nitride (UN) cermet. There is an extensive data for the performance of the UN fuel; in fact, molybdenum UN cermet was one of the original fuel forms investigated for NTP applications. Experimental fabrication of Mo-UN cermets achieved up to 98% of theoretical density [21]. One of the key advantages of UN is the increased uranium-235 loading density. Additionally, the thermal conductivity of UN increases as temperature increases. UN and UO_2's thermal conductivities are presented in Figure 3.3. The advantage of UN becomes apparent for high temperature systems. The thermal conductivity correlations for UN and UO_2 are detailed in chapter 4. Mo-UN fuel systems have also been considered for micro-reactor applications for their desirable thermal characteristics [22].

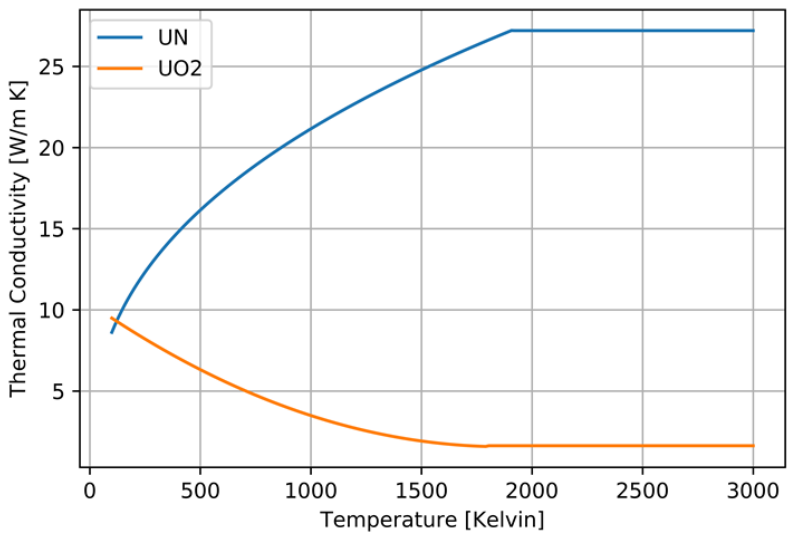

Figure 3.3 UO_2 and UN thermal conductivity comparison.

The melting temperature of UN is a function of the nitrogen overpressure. Fabrication of UN fuel in a nitrogen rich stoichiometry can increase the nitrogen vapor pressure at evaluated temperatures yielding a higher melting temperature. The recommended nitrogen to uranium ratio is 1.04. In this thesis, a nitrogen to uranium ratio of 1 is used [23]. Recent research and development efforts [24] and small business innovation research solicitations [25] have focused on dispersion strengthened molybdenum/tungsten alloys. Recent work published by NASA evaluating the thermal hydraulic performance of LEU NTPs has utilized a Mo-30W alloy, the same alloy is adopted in this thesis for the high temperature region of the fuel [26].

3.1.2 Moderator Elements

As was stated in section 3.1.1, the selected fuel uses LEU kernels, and therefore heritage designs cannot be directly used. The significantly lower uranium-235 loading leads to a sub-critical reactor-core configuration, unless sufficient moderation is provided. A critical configuration is obtained by placing enough moderating elements in the active core region to achieve a softer neutron spectrum. Figure 3.4 presents the radial cross section of the moderator element design and describes each region. The hydrogen flow makes two passes through the moderator element. The first pass, typically referred to as the supply channel, cools the interior ZrH_x of the moderator element. The second pass, referred to as the return channel, cools both the internal and external structures of the moderator elements. The dual pass flow configuration is the key design feature that enables the use of an expander cycle, which is detailed in Figure 3.4. The return channel reverses the direction of the hydrogen flow back out of the core, where the heated hydrogen feeds to a turbine to

provide power for the main pump. Table 3.2 lists the geometry parameters for the moderator element used in this study.

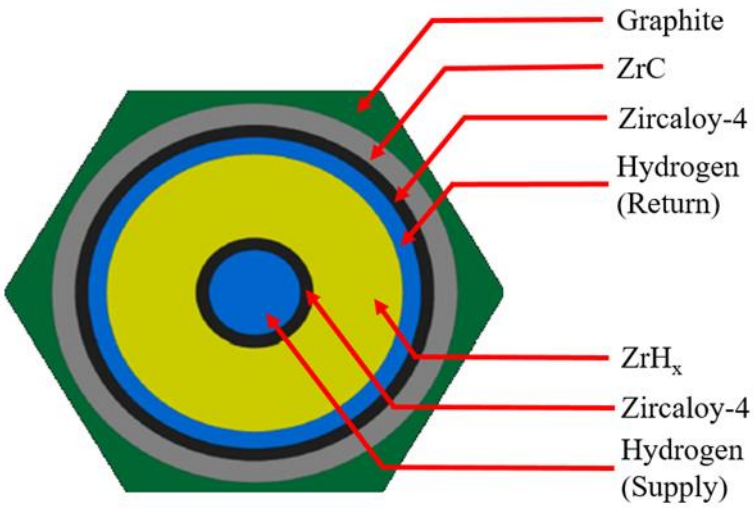

Figure 3.4 Moderator Element Geometry

Table 3.2 Moderator Element Geometry Parameters

	Unit	**Value**
Moderator Element Flat to Flat	cm	1.905
Moderator Element Supply Coolant Channel Radius	cm	0.2
Moderator Element Supply Channel Cladding Thickness	cm	0.057
Moderator ZrHx Thickness	cm	0.393
Moderator Return Channel Thickness	cm	0.08
Moderator Return Channel Cladding Thickness	cm	0.057
Moderator Insulator Thickness	cm	0.103

The role of the moderating element is to provide moderating power and slow down the neutrons, while thermally insulating the zirconium hydride layer due to its lower thermal margin to failure. Zircaloy-4 is employed in both the inner and outer tie-tubes which provide support for the moderating element. Zircaloy-4 was chosen over the Inconel-718 used in NERVA designs due to its lower thermal neutron capture cross section. The inner and outer tie-tubes are designed to transfer the forces resulting from the core's

pressure drop to the cold end support plate and isolate the fuel elements from tensile stress. The zirconium hydride ring within the moderating element performs the actual moderating role. While hydrogen migration in the moderator is a concern and can act as thermal limitation [27], it has not been considered in this thesis's analysis. Recent research conducted by Los Alamos National Lab has investigated the use of yttrium hydride as a replacement for zirconium hydride due to its increased stability at higher temperatures [28]. However, this research is still in the early stages of development; therefore, ZrH_x has been chosen as the moderator material for this thesis.

The main insulation that shields the ring of zirconium hydride from the high temperatures of the fuel elements is provided by a layer of porous zirconium carbide. By decreasing the density of the ZrC, its thermal conductivity is decreased by more than a factor of 50, creating a large temperature gradient across the zirconium carbide. Additionally, graphite is susceptible to hot hydrogen corrosion, so the layer of ZrC shields the graphite from any hydrogen contact. The outermost ring of the moderating element features graphite, which has a high thermal conductivity, ensuring sufficient thermal margins of the graphite region.

3.2 Core Configuration

3.2.1 Radial Core Configuration

Figure 3.6 presents a detailed cross section of the reactor core radial configuration. A graphite sleeve surrounds the active core, followed by a void (denoted by a grey color), a zirconium carbide insulator (black color), an Al-2024 inner pressure vessel (white color),

a beryllium radial reflector (gold color) with boron carbide control drums (brown color) embedded within, and an Al-2024 outer pressure vessel (white color).

The graphite sleeve acts as the core former and provides lateral support as the increases in temperature and expands. Additionally, the graphite provides another layer of moderating material to thermalize the neutron flux before interacting with the inner pressure vessel and radial reflector. The zirconium carbide (ZrC) ring is the insulator between the graphite sleeve and inner pressure vessel. This ring provides a thermal barrier and protects the vessel from the high core temperatures. The beryllium radial reflector tends to elastically scatter neutrons, and undergoes a (n,2n) reaction producing additional neutrons. The radial reflector significantly reduces the leakage of neutrons, which reduces the critical size of the core allowing for increased thrust to weight ratios. The pressure vessel needs to be composed of a material that can withstand the very high pressures within the core. Al-2024 has a very high ultimate tensile and yield strength [29], allowing it to resist fatigue due to high pressures. In addition, Al-2024 possesses neutral neutronic characteristics. Excess core reactivity is controlled by sixteen radially distributed control drums located inside the radial reflector. One third of the control drums outside surface contains boron carbide enriched to forty percent boron-10, the primary neutron absorber in boron. Boron carbide, one of the hardest known materials, was the absorber of choice due to its ability to absorb neutrons without forming radioactive isotopes with long half-lives. Figure 3.6 displays the control drums rotated, full out, 180° to the core. The control drums with be rotated out during the analysis presented in this thesis in order to induce the maximum reactivity of each core.

In previous HEU NTP designs the core pattern was fixed and radial power peaking was suppressed by radial zoned uranium enrichment, this is not done in LEU NTP's. In order to maximize the amount U-235 in the core, radial peaking is managed by the arrangement of the moderator elements inside the core. Several different moderator and fuel element patterns can be used in a single core, Figure 3.5 shows the three different lattice patterns used to generate variable ME:FE ratio cores. Figure 3.6 shows an example of the full core radial configuration using the bullseye pattern and inverse-pewee pattern.

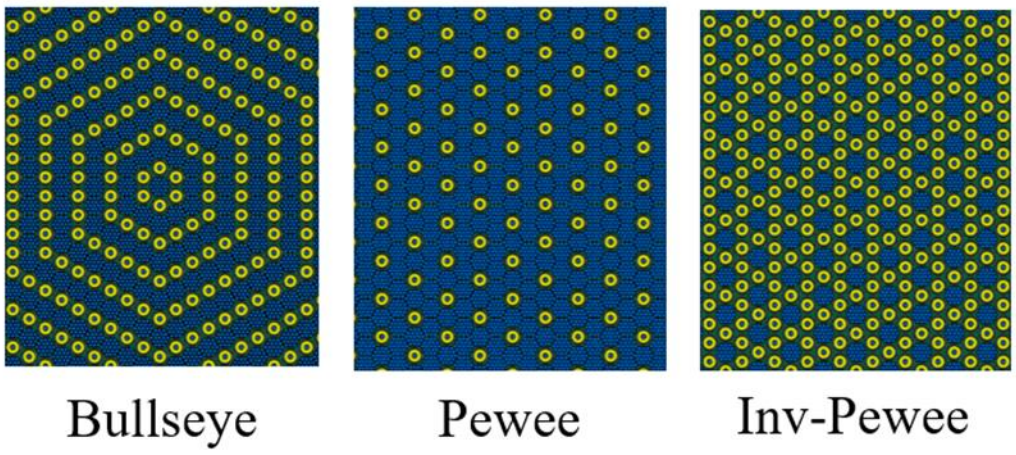

Figure 3.5 Active Core Patterns

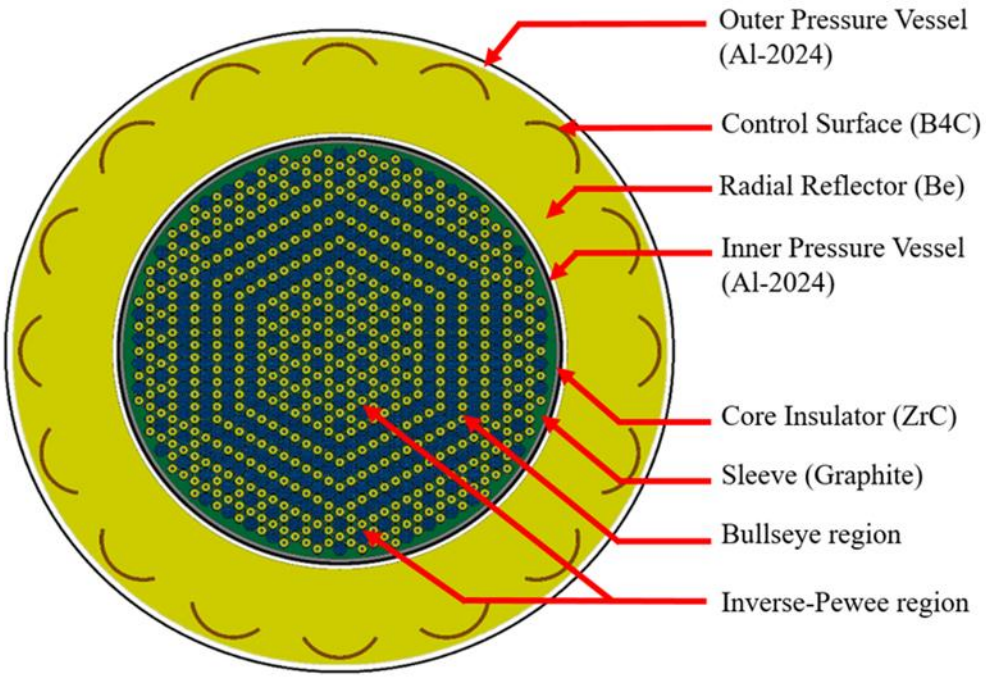

Figure 3.6 Radial Core Configuration Example

3.2.2 Axial Core Configuration

A detailed axial configuration is presented in Figure 3.7 which also describes the various materials and regions of the active core regions.

An axial beryllium oxide (BeO) reflector is placed above the active core region to reduce neutron leakage. The use of pure beryllium in this region of the core is not possible due to the high energy deposited from the active core, and elevated gas temperatures entering the core. Therefore, a material with a higher melting temperature is required. The

melting point of BeO is 2780 K, which is more than satisfactory for the flow conditions present in the axial reflector.

Above the axial reflector and surrounding the supply and outlet plena is another support plate made of Al-2024. This material was selected due to its excellent mechanical properties. The plena directs the flow of hydrogen in the moderator supply and return channels. The hydrogen passes through the core twice in the moderator elements, gaining the required energy to power the turbine.

The lithium hydride and tungsten shielding lie above the inlet plena and support plates. The lithium within the neutron shield is enriched to contain nearly 100% Lithium-6, which undergoes thermal neutron capture via the (n,α) reaction. The (n,α) reaction does produce tritium, but this specific issue is not addressed in this thesis. The gamma shield is composed of tungsten. Alternate shielding materials have been investigated during the NERVA program such as Boron carbide Aluminum and Titanium Hydride (BATH) shielding [30]. Currently, no strict neutron flux or gamma dose requirements are available since these limits are driven primarily by the flux limits of the mechanical components above the core, such as the turbo-pump machinery, pressure transducers, and control drum drives [30]. Shielding analysis are considered outside the scope of this thesis; however, investigation of the component fluence limits could lead to a significant reduction of total engine mass.

The active core region is split into an upper and lower region in this study similar to the ANL-200 design, where the upper region of the core will utilize a molybdenum matrix material and the lower region of the core will utilize a dispersion strengthened molybdenum

tungsten alloy. The height (*i.e.*, axial location) where this core is split will be one the major parameters evaluated in this study.

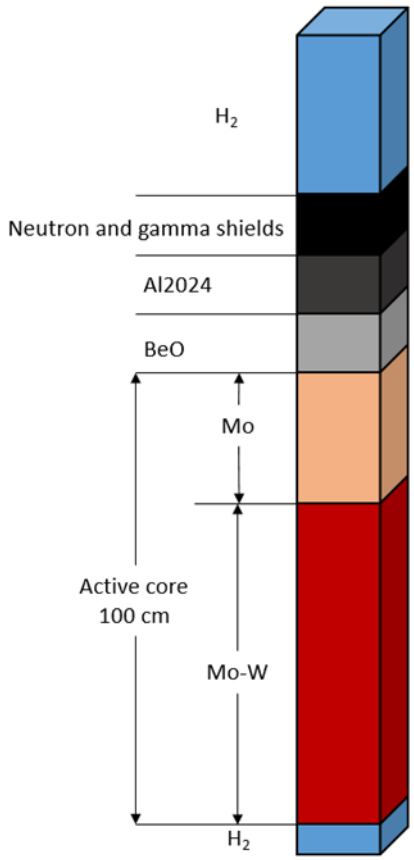

Figure 3.7 Core Axial Configuration

3.3 Expander Cycle

The SNRE design initially considered the use of an expander cycle, and subsequent analysis performed by NASA Glenn Research Center [31] showed that the application of an expander cycle can greatly increase NTP performance. Two main classes of engines were considered in previous analysis, small and large engines. The main distinguishing characteristic between the two classes is the total system mass flow rate, and subsequently

the thrust produced. Each engine class is typically analyzed using a specific turbo-pump configuration. The small engine class utilizes the RL-10 hydrogen pump and turbine, while the large engine class utilizes the RL-60 hydrogen pump and turbine. The hydrogen pump and turbines are limited by their maximum flow rate, the RL-10 has a maximum flow rate of approximately 4 kilograms per second, while the RL-60 has a maximum flow rate of approximately 12 kilograms per second. Since the expected mass flow rate of 25 klb_f rocket is approximately 13 kilograms per second, a dual turbo-pump assembly is used in the large engine configuration. This configuration is represented by Figure 3.8.

The expander cycle begins at point 1 labeled in Figure 3.8. At this point, the hydrogen from the main propulsion tank enters the pump and becomes highly pressurized, the flow then proceds to point 2. It is at this point that the flow is split, part of the flow is directed to the nozzle coolant skirt and reflector circuit, the remaining flow is directed to the moderating supply and return circuit. In this study, the fraction is refered to as the moderator flow fraction. This number is always between zero and one, where larger numbers represent more flow being directed to the moderator element circuit. At point 3r the hydrogen flow enters the cooling skirt gaining energy, and then enters the reflector region at point 4r and exits the reflector at point 5r. The moderator supply channel begins at point 2m where the proppelant flows through the supply channel. The flow then turns around at point 3m and travels through the moderator return channels and exits the active core region. These two circuits recombine at point 6, the total flow is then sent to the turbines. Half of the total flow is sent to each turbine, where part of the flow bypasses the turbine based on a pre-determined maximum mass flow rate. The remaining flow travels across the turbine losing energy and cooling. The bypass flow and turbine flow recombine

at point 8 and then the total system mass flow enters the fuel element channels. The hydrogen is then super heated by the fuel element flow channels and is then expelled through the nozzle at point 10 providing thrust.

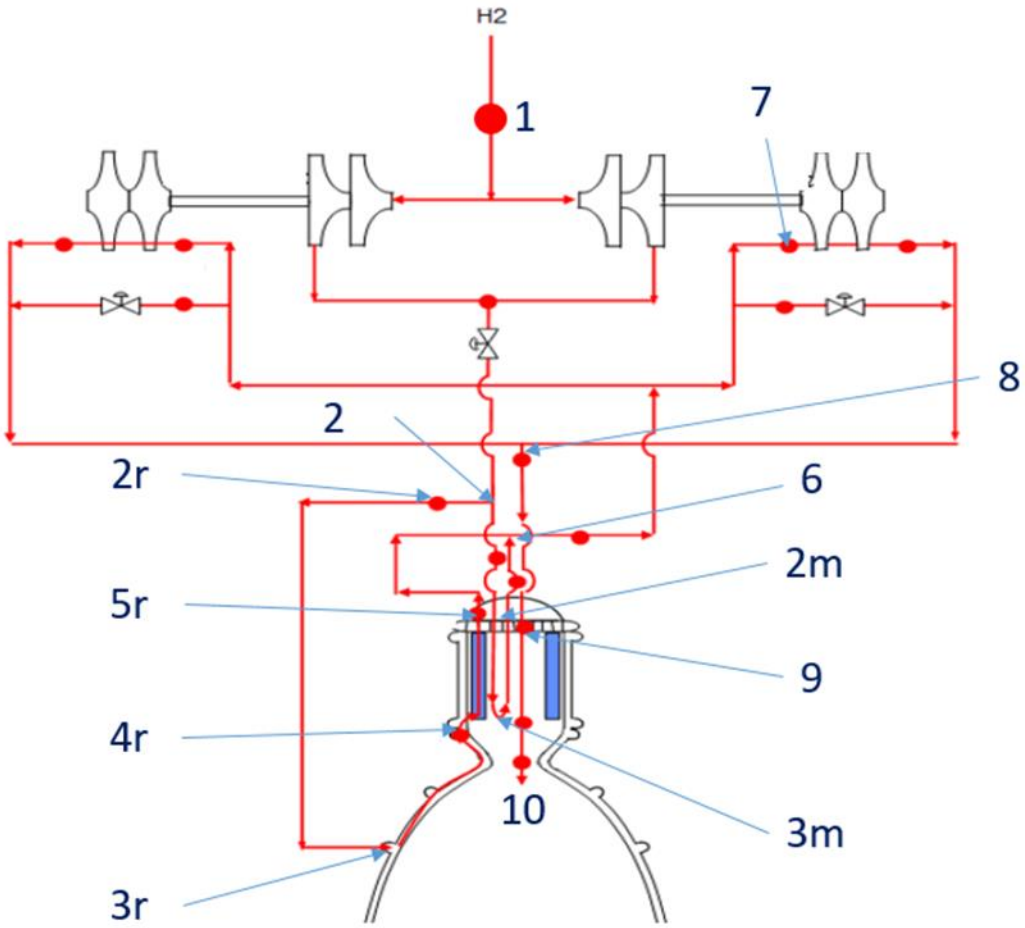

Figure 3.8 Large NERVA expander cycle [31]

The cycle described in this section will be applied to all systems in the analyses presented in this thesis.

CHAPTER 4. CODES/COMPUTATIONAL METHODS

The Monet Carlo based, Serpent, code is used for all neutronics calculations and is described in section 4.1. The thermal hydraulic (T/H) methodology developed and implemented in our in-house, NTP-THERMO, code is described in section 4.2. The T/H problem is considerably more challenging for NTP designs that employ the expander cycle compared to traditional commercial LWR systems due to the irregular counter flow that exists in the active core. Therefore, a designated section to describe the heat transfer from the fuel element to the moderator element is described in section 4.3. A methodology was developed here to study the variation in pressures and temperatures of the complete integrated system (e.g. turbines, pumps, core, reflectors, nozzles). The methodology was implemented in the POWER framework and is described in section 4.4. The thermal properties for hydrogen and all the materials that were included in the engine design are described in section 4.5, and the nozzle performance code is described in section 4.6.

4.1 Serpent

Serpent is a multi-purpose three dimensional (3D) Monte Carlo particle transport code developed at the VTT Technical Research Centre of Finland. Serpent allows for the modelling of complex irregular 3D geometries, which is an extremely advantageous feature for advanced NTP designs. Originally, Serpent was designated as a tool for generation of homogenized few-group constants. However, Serpent is continuously being developed and applied to study advanced systems due to the recent implementation of a multi-physics interface. All of the neutronic analysis presented in this thesis were performed with the Serpent code [32]. Serpent has been extensively verified [33], and its range of applicability

is greatly increasing [34]. The code achieves more efficient CPU time performance due to the code's implementation of Woodcock delta-tracking [35] of particles. In our current study, ENDF/B-VII.0 evaluated data library was used [36]. Recent releases of the code have included coupled neutron and gamma transport capabilities [37]. These capabilities were enabled to account for the gamma heating effect on the shape of the axial power profiles used in T/H sub-channel analysis. While the total amount of energy deposited by gamma rays is a small fraction of the total reactor power it does have a unique effect on the power shape. Since the mean free path of gamma rays is much larger than that of neutrons the gamma heating slightly flattens the axial power profile, which can have a minor, but non-negligible, effect on a specific rocket's I_{sp}.

4.2 NTP-THERMO

The THERMO code module was originally developed for light water reactor thermal hydraulic analysis. The work presented in this thesis used a specifically adapted version of THERMO for NTP analysis (NTP-THERMO). One of largest modifications made to THERMO was the development of a mesh-based resistance network and the implementation of a numerical solution to the radial conduction problem. This approach was used due to the heat transfer coefficient dependence on the fuel surface temperature and bulk temperature.

4.2.1 Calculation Sequence

The main calculation sequence was designed to process multiple flow channels and equalize the pressure drop across each channel by iterating on the mass flow rate of each channel. Figure 4.1 presents the main calculation sequence of NTP-THERMO. The code

can be executed using an input and output card system or can be directly fed data from an external program. Additionally, the resulting data can either be printed to an output file or written to a binary file for an external program to parser and analyse. The code was developed to be versatile and able to handle the various designs considered in this thesis.

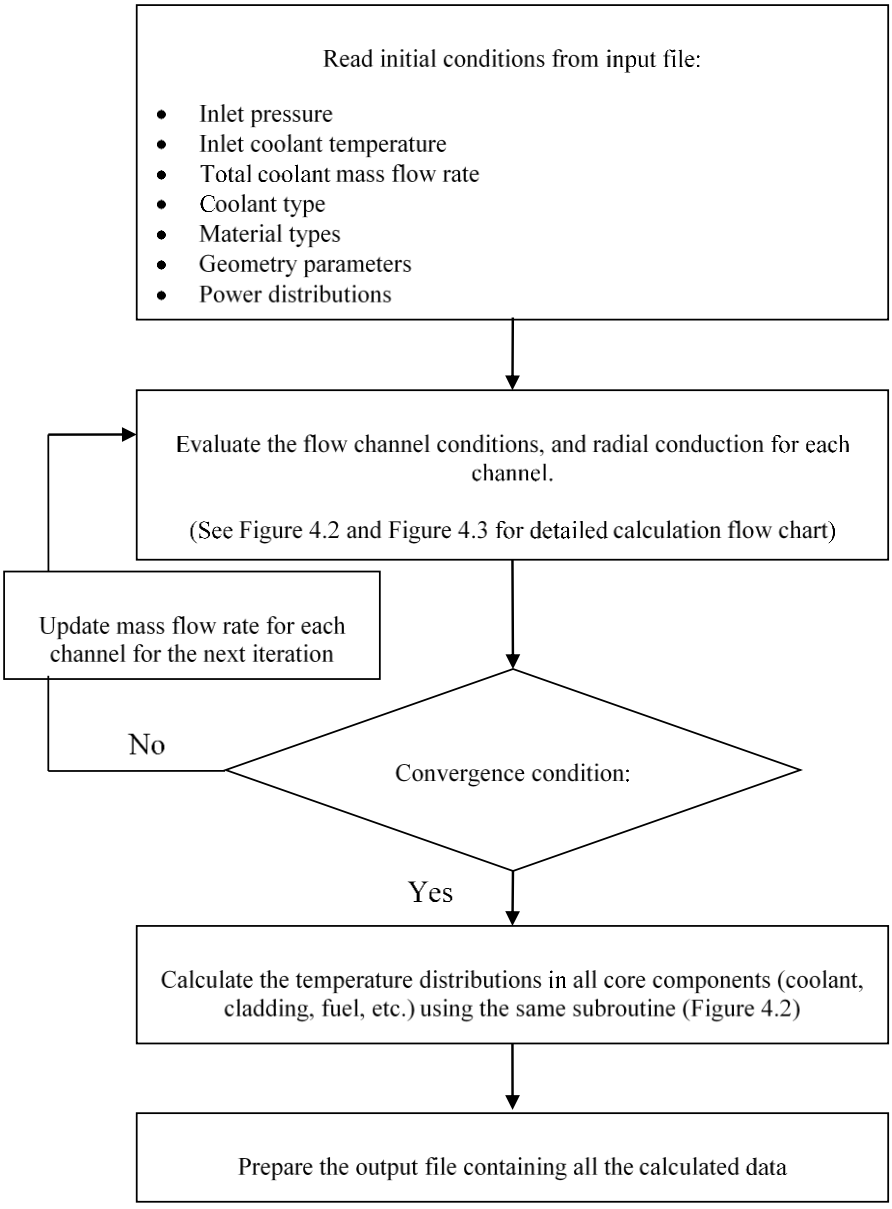

Figure 4.1 NTP-THERMO Main Calculation Sequence

Figure 4.2 details the flow channel solution used in NTP-THERMO for calculating the hydrogen flow conditions, all of the hydrogen property calculations are a function of pressure and temperature. All of the solid material properties are a function of temperature.

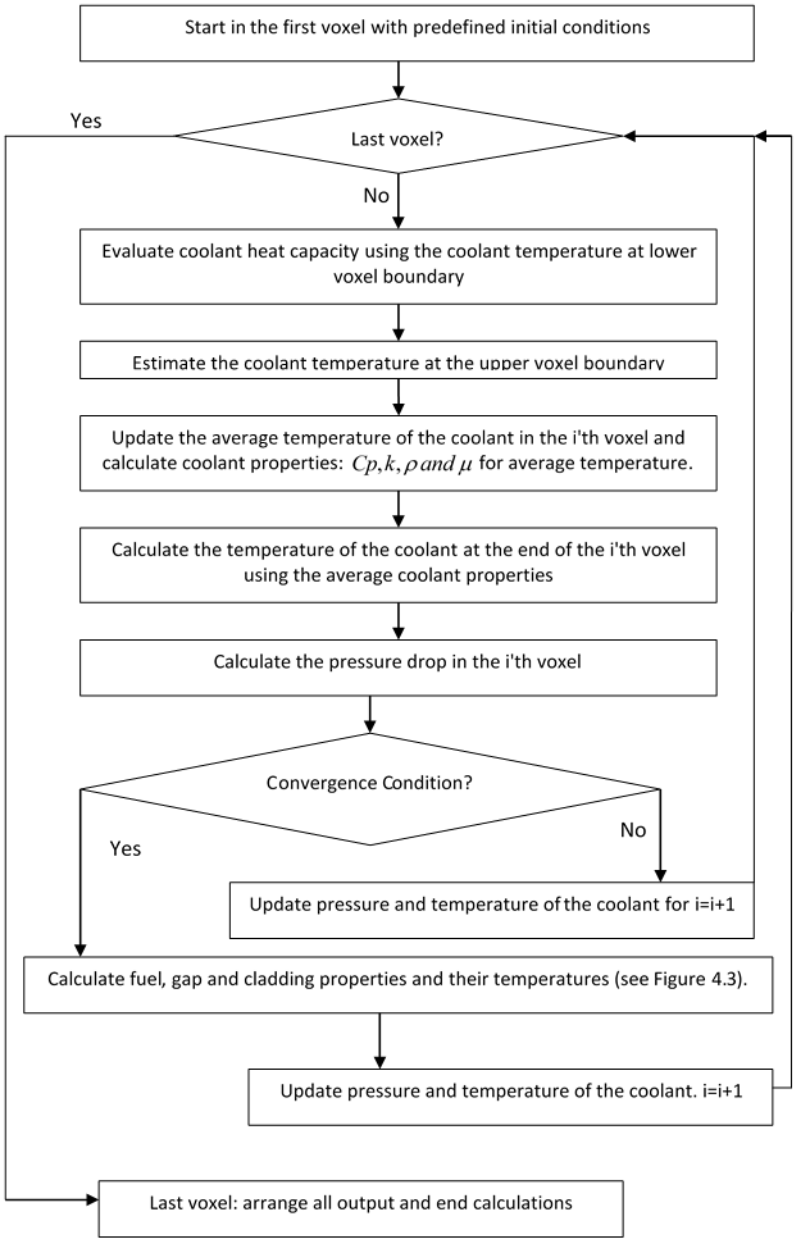

Figure 4.2 NTP-THERMO Flow Calculation Sequence

Figure 4.3 detailed the radial conduction calculation sequence. This loop is required due to the heat transfer coefficient's dependence on the bulk coolant temperature.

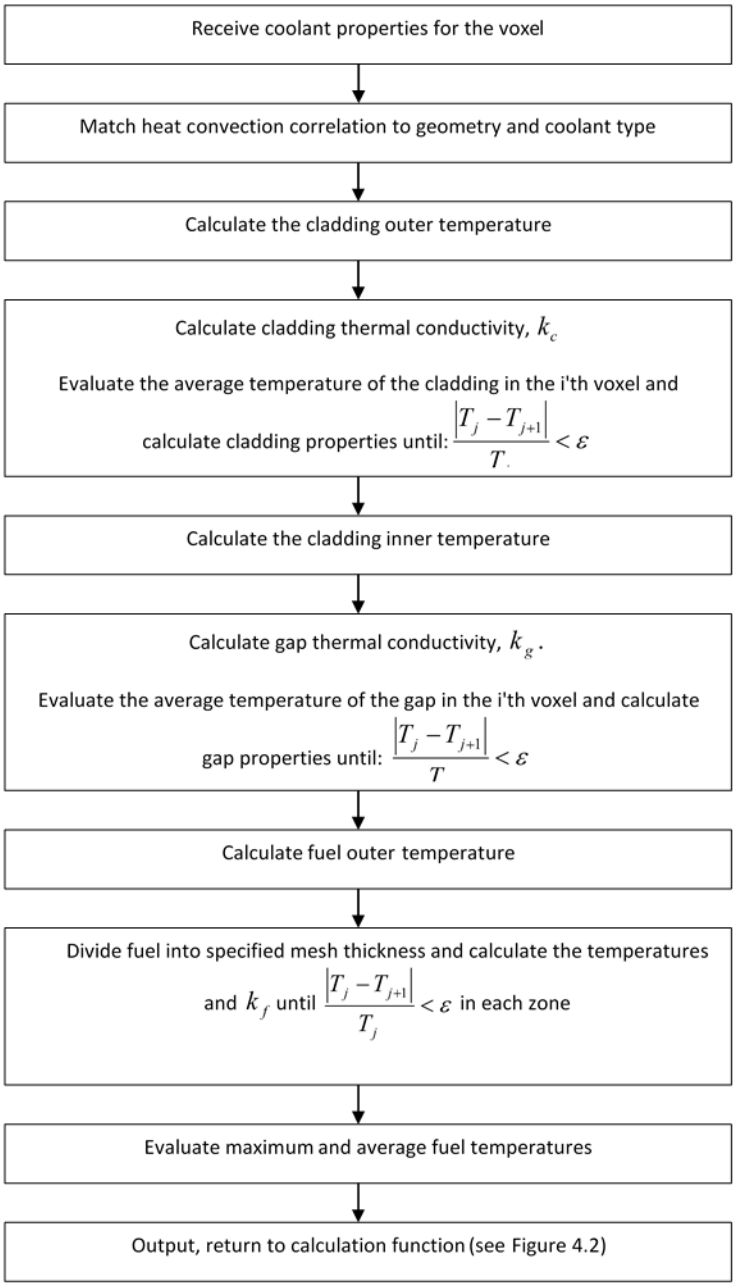

Figure 4.3 NTP-THERMO Radial Conduction Calculation Sequence

4.2.2 Radial Conduction Model

A finite difference model was used to solve the steady-state conduction model [38]. The formulation relies on the resistance model, where the temperature in each node *i* is obtained by considering the heat transfer between multiple adjacent nodes. The wall temperature of the outer node is calculated according to the bulk temperature of the hydrogen with known flow characteristics at a specific axial layer. Equation 4.1 presents the formulation for calculating the temperature of a node *i,* where q_i is the heat produced in node *i*, R_{ij} is the resistance between nodes *i* and *j*.

$$T_i = \frac{q_i + \sum_j \frac{T_j}{R_{ij}}}{\sum_j \frac{1}{R_{ij}}} \qquad \text{Equation 4.1}$$

In the analysis presented in this thesis, node *i* has only two adjacent neighbors, the left (R_{i-}) and right side (R_{i+}) resistances. The equivalent annulus is discretized into radial layers with a thickness of Δr_i. The volume of each element *i* is $\Delta V_i = r_m \Delta r_i \Delta\theta \Delta z$. The heat produced in a specific layer *i* can be determined by product between the power density and the corresponding volume in layer *i.* In a cylindrical coordinate system, the conduction resistances are calculated using Equation 4.2.

$$R_i = \frac{\Delta r_i}{\left(r_m \pm \frac{\Delta r_i}{2}\right) \Delta\theta \Delta z} \frac{1}{k_{i\pm}} \qquad \text{Equation 4.2}$$

The outer most node, $i = N$, of the resistance series is modified to account for any slight differences between the mesh structure and geometry of the given problem. The resistance term is modified in accordance with Equation 4.3.

$$R_{N+} = \frac{\Delta r_N/2}{\left(r_m \pm \frac{\Delta r_N}{4}\right)\Delta\theta\Delta z}\frac{1}{k_{i\pm}} \qquad \text{Equation 4.3}$$

Combing the relations in to a matrix format, the following tri-relation can be written:

$$\begin{bmatrix} \frac{1}{R_{1-}} - \frac{1}{R_{1+}} & -\frac{1}{R_{1+}} & 0 & 0 & \cdots & 0 \\ -\frac{1}{R_{2-}} & \frac{1}{R_{2-}} + \frac{1}{R_{2+}} & -\frac{1}{R_{2+}} & 0 & \ldots & 0 \\ \vdots & \cdots & \ddots & \ddots & \ldots & \vdots \\ 0 & \ldots & 0 & -\frac{1}{R_{(N-1)-}} & -\frac{1}{R_{(N-1)-}} + \frac{1}{R_{(N-1)+}} & -\frac{1}{R_{(N-1)+}} \\ 0 & \ldots & 0 & 0 & -\frac{1}{R_{N-}} & \frac{1}{R_{N-}} + \frac{1}{R_{N+}} \end{bmatrix} \begin{bmatrix} T_1 \\ T_1 \\ \vdots \\ T_{N-1} \\ T_N \end{bmatrix} = \begin{bmatrix} q_1 \\ q_2 \\ \vdots \\ q_{N-1} \\ q_N + \frac{T_b}{R_{N+}} \end{bmatrix}$$

In this formulation, the temperature of the outer surface is represented by T_b and is set as the bulk hydrogen temperature of each axial layer. In order to account for temperature dependent thermal conductivities, the implementation relies on an iterative solution scheme, in which the thermal conductivities are initially guessed according to a uniform nodal temperature distribution$[T_1 \quad T_1 \quad \ldots \quad T_N]^T = T_b$. Once the nodal temperature distribution is calculated, it is reapplied to update the conductivity values and therefore the resistances. This iterative methodology is repeated until a convergence of $\Delta T_i < 0.5℃$ in all nodes is achieved.

The heat transfer coefficients are typically correlated using the Nusselt number as a way to measure the convective heat transfer at the wall. The NASA Glenn research center

developed a general Nusselt number correlation formula for gas flowing through a heated pipe, which included a correction term that accounted for the ratio of the surface wall temperature to bulk hydrogen temperature [6]. Equation 4.4 presents the general correlation, where T_w is the surface is wall temperature of the coolant channel, and T_b is the bulk coolant temperature.

$$Nu = C_1 \times Re_b^{C_2} Pr_b^{C_3} \times (T_w/T_b)^{C_4} * (C_5 + C_6 * (X/D)^{C_7})^{C_8} \qquad \text{Equation 4.4}$$

The Taylor Nusselt number correlation was used to calculate the heat transfer coefficient in the fuel element flow path. Taylor's correlation has been printed in several different publications, some of which are inconsistent. Equation 4.5 presents the correct correlation.

$$Nu = 0.023 \times Re_b^{0.8} Pr_b^{0.4} \times (T_w/T_b)^{-0.57-1.59*x/D} \qquad \text{Equation 4.5}$$

The Petuhkov heat transfer correlation, presented in Equation 4.6, was used to calculate the heat transfer coefficient in the moderator element flow path.

$$Nu = 0.0212 \times Re_b^{0.8} Pr_b^{0.4} \times (T_w/T_b)^{-C*x/D} \qquad \text{Equation 4.6}$$

$$C = 0.55 \quad \frac{x}{D} < 75$$

$$C = 0.135 + 0.005548 * x/D \quad \frac{x}{D} \geq 75$$

4.2.3 Axial convection and pressure drop models

Axial heat conduction was ignored in the solid fuel regions and the conduction from the fuel to the hydrogen coolant was only considered in the radial direction. The hydrogen bulk temperature was updated for each axial layer using Equation 4.7.

$$T_{\infty(out)} = T_{\infty(in)} + \frac{V}{\dot{m}C_p} q''' \qquad \text{Equation 4.7}$$

Where $\dot{m}$ is the mass flow rate of hydrogen, q''' is the power density in volume V, C_p is the heat capacity of the hydrogen, and T_∞ is the bulk hydrogen temperature. The inlet temperature, $T_{\infty(in)}$, of the axial layer is set as the outlet temperature $T_{\infty(out)}$ of the previous node. The heat balance in each node is visualized in Figure 4.4.

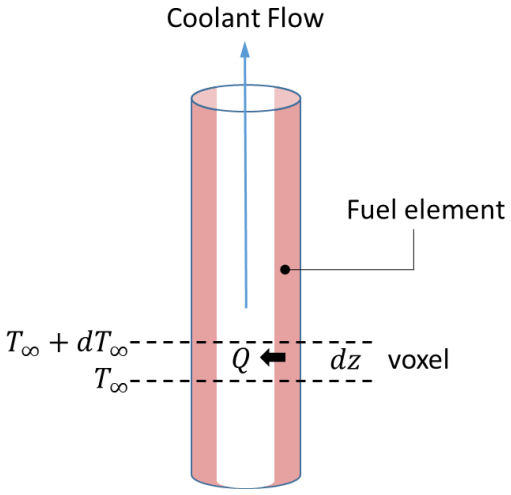

Figure 4.4 NTP-THERMO Heat Balance

Friction, form, and acceleration pressure losses are all accounted for in the T/H analysis. Equation 4.8 shows the pressure loss term calculated in each node, where f is the friction factor, dz, is the length of the node, De_H is the hydraulic diameter, and v is the

fluid velocity. Gravity losses are neglected in this analysis due to the rocket engine operating in space.

$$P_{out} = P_{in} - \frac{f dz}{De_H \rho \, {v^2}/{2}} - (\rho v^2 - \rho v) \qquad \text{Equation 4.8}$$

The pressure losses from friction are highly dependent on the friction factor correlation used in the calculation. Analysis conducted at Lewis Research Center [40] developed the ELM Program for rapid T/H analysis of solid core nuclear rockets to support the Space Exploration Initiative outlines several friction correlations. Equation 4.9 presents the friction factor correlation used to calculate the friction pressure losses.

$$f = 0.25 \times (0.0345 + {363}/{Re_b^{1.25}}) \qquad \text{Equation 4.9}$$

4.3 Fuel Element to Moderator Element Heat Transfer

The heat transfer problem of the fuel element and moderator element is challenging as the propellant flows in two opposite directions within the ME and then exits and mixes with the flow from the reflector/nozzle section. Therefore, the inlet boundary conditions to the FE are highly dependent on the ME, however the latter requires a prior knowledge of the temperature distribution within the FE to accurately predict the heat transfer to the ME.

In order to obtain the temperature and pressure distribution within the fuel and moderating elements, each T/H channel was split into three separate T/H channels (*i.e.*, supply, return and fuel). The converged solution is obtained via the iterative computational

scheme presented in Figure 4.5 . The inlet conditions to the supply channel are well known and are not dependent on either the return or fuel channels. In the analysis presented, the supply channel was decoupled from the rest by assuming that the heat generation within the ZrHx element is transferred predominantly to the coolant that flows at the center of the ME due to the considerably lower interior temperatures as opposed to the exterior wall (e.g. return channel). This assumption is not entirely accurate, but is conservative in predicting higher centerline temperatures within the ZrHx region. Following this channel solution, the supply outlet conditions are set as the inlet conditions to the return channel. In addition, the fuel element is solved independently with approximated inlet conditions to obtain the fuel centerline temperature axial distributions, which are then also used in the solution of the return channel as the wall boundary conditions. The outlet temperature and pressure from the return channel solution are used in conjunction with the outlet conditions obtained by solving the heat transfer problem in the reflector and nozzle (not shown in Figure 4.5). The mixed conditions are then set as the inlet boundary conditions to the fuel element and the procedure is repeated until a convergence in fuel element inlet conditions is achieved.

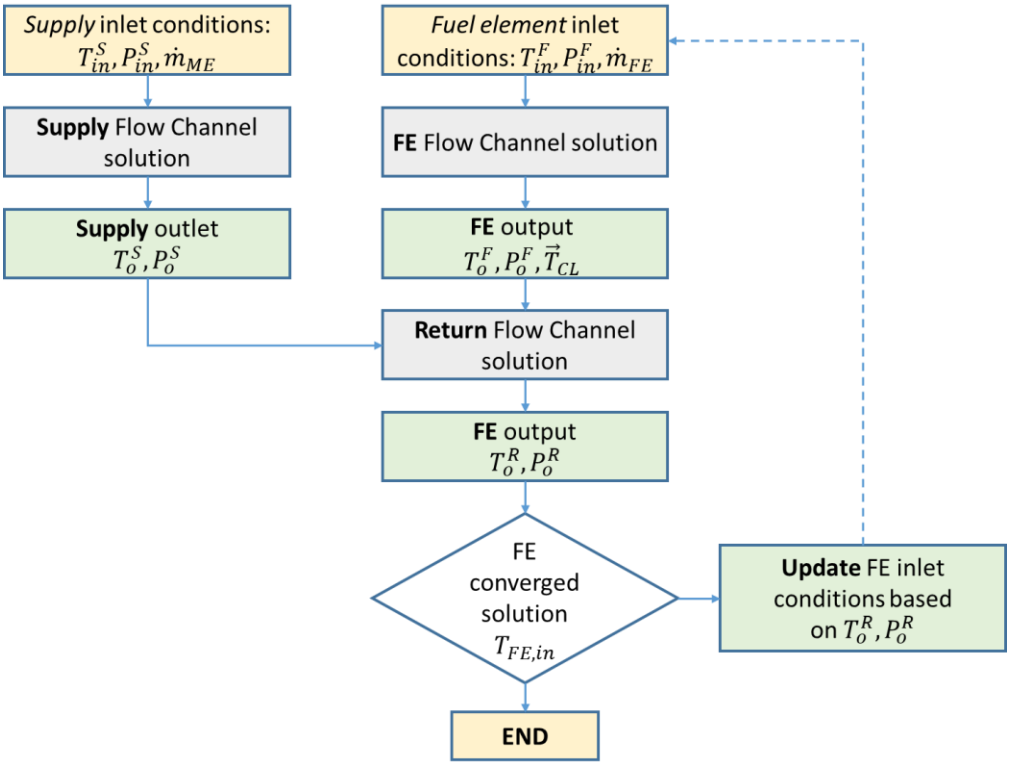

Figure 4.5 Fuel to Moderating Element Heat Transfer Solution

4.4 POWER

4.4.1 Calculation Sequence Description

The in-house developed, POWER, computational framework relies on an iterative method to converge all state points of the expander cycle while evaluating the heat transfer between the moderator and fuel elements.

The POWER script contains four iterative loops. The first loop converges the fuel element inlet conditions, the second loop adjusts the total reactor power to ensure that the specified maximum centerline fuel temperature is not exceeded, the third loop adjusts the pump power to achieve a specified chamber pressure, and the fourth loop adjusts the system

mass flow rate to achieve specified exit Mach number. Each one of these loops can be executed independently of each other, which allows the code to perform a variety of engineering analysis. Figure 4.6 presents the main calculation flow diagram, and Figure 4.7 presents the boundary conditions convergence calculation sequence. Similar to the THEMRO code, POWER also uses an input and output file system. All three outer loops can be activated simultaneously, but may require several outer loop iterations which can results in calculation times on the order of 10 minutes for a final converged solution, which makes the script a modest computational cost tool. With further function optimization, it is expected that the calculation time can be significantly reduced. This is an engineering-based tool that allows to identify a set of operational conditions (e.g. power) while satisfying the constraints set by the user (e.g. maximum Mach number). The iteration loops have the ability to over-ride some initial input user information such as the total reactor power, pump power, and total system mass flow rate to achieve the specified target parameters. For example, when the code is iterating on the desired temperature margin set by the user, the total reactor power will be adjusted until the margin to maximum centerline temperature reaches zero in the most limiting node. The user's input target chamber pressure will over-ride the pump power to achieve either a higher or lower exit pump pressure to satisfy the chamber pressure. The target Mach number will over-ride the input mass flow rate to achieve the specified Mach number. The pump function calculates the hydrogen flow conditions after exiting the pump and then pressure drop from friction losses in the system piping connecting the pump to the nozzle and moderator element inlet. The total system mass flow rate is then split based on a user input, referred to as the moderator flow fraction. Part of the total flow directed to the nozzle regenerative cooling skirt and

then passes through the reflector. The remaining flow enters the moderator supply channel. The moderator and fuel element flow channels are solved using the THERMO code while accounting for the heat transfer from the fuel to the moderator. This yields the hydrogen flow conditions exiting the moderator return channels. The moderator return flow is then mixed by the mixing chamber function with the flow exiting the reflector circuit and then enters the turbine. Part of the flow bypasses the turbine, while the rest of the flow passes across the turbine losing enthalpy and providing the required pump power. The pump power and turbine efficiency determine the amount of enthalpy lost by the hydrogen in the turbine. The flow exiting the turbine is then mixed with the bypass flow. The recombined flow undergoes a pressure drop from the pipe losses function. The resulting flow conditions are set as the fuel element inlet conditions which are used to update the guessed fuel element conditions. This calculation loop is repeated until the calculated fuel element conditions and guessed fuel element have converged. Once the fuel element inlet conditions have converged the reactor power is adjusted to ensure that the maximum centerline fuel temperature is not exceed in any of the fuel element nodes. This process requires the fuel element inlet conditions to be re-assessed with each adjustment of the total reactor power.

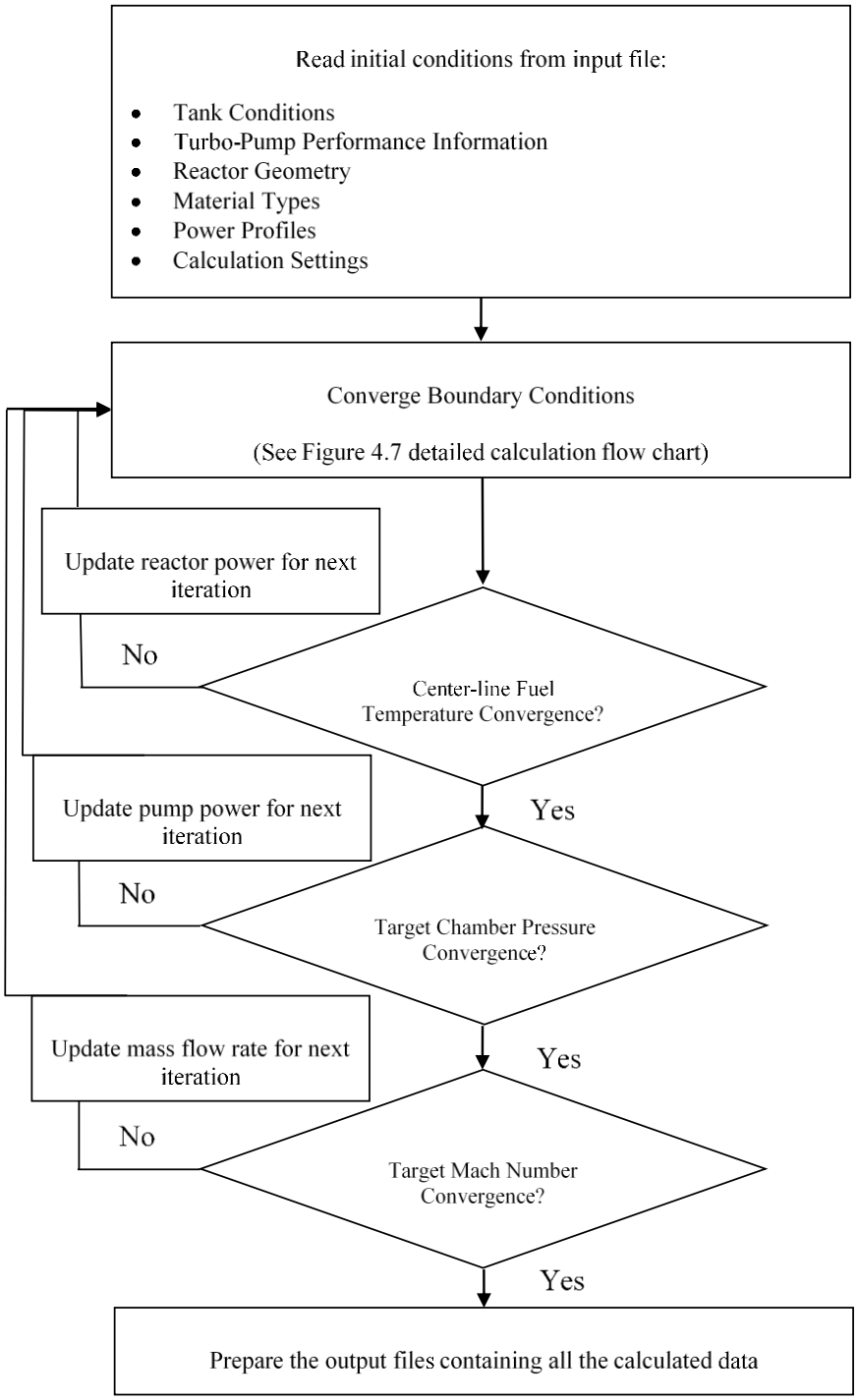

Figure 4.6 POWER Main Calculation Sequence

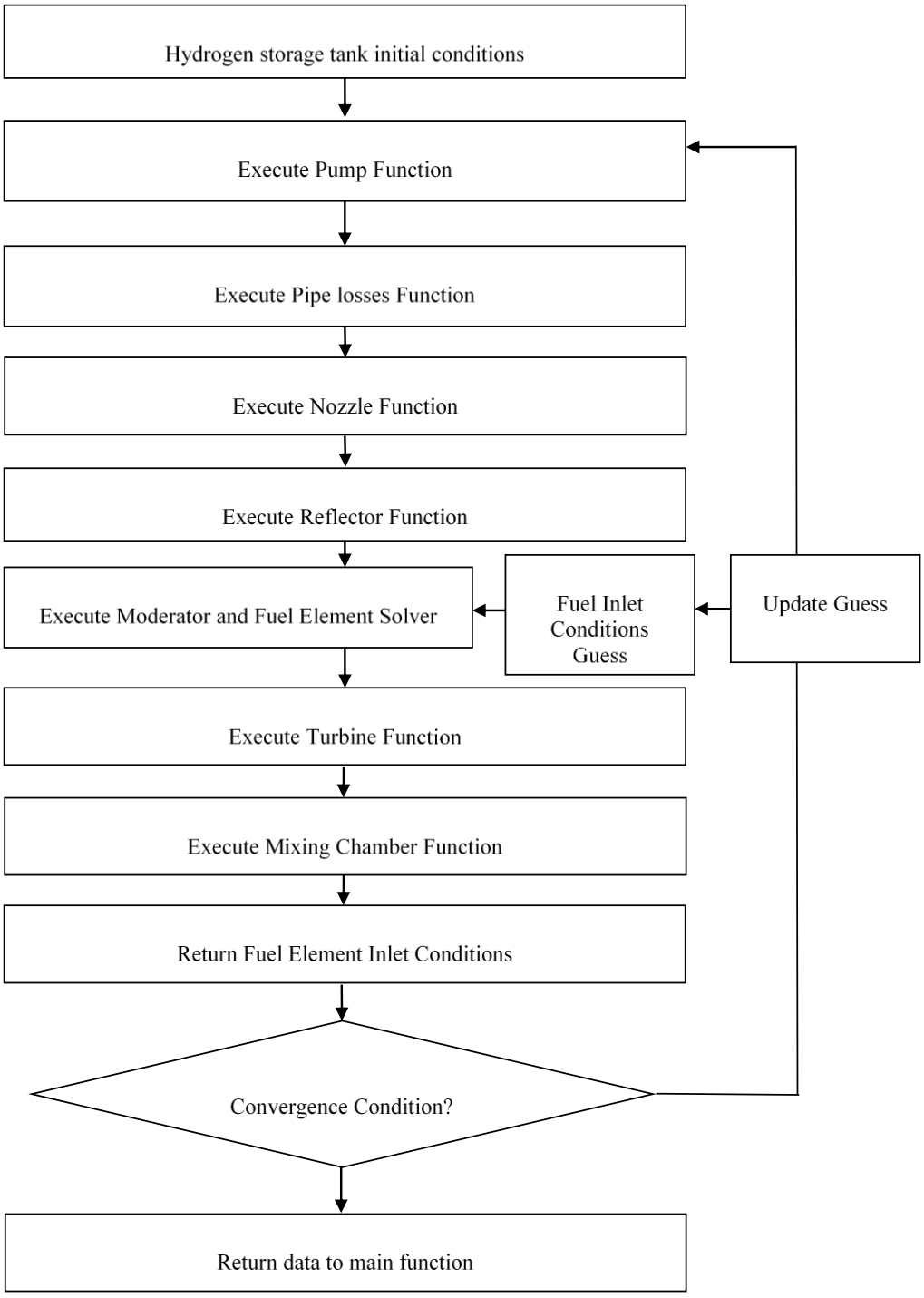

Figure 4.7 POWER Boundary Conditions Calculation Sequence

4.4.2 POWER Sub Functions

The pump in an NTP system provides the driving pressure to move the coolant through the expander cycle. Since the mass flow rate of the system and inlet conditions are known, the pump exit conditions can be solved. The change in coolant pressure can be calculated by multiplying the pump head, *h*, by the inlet fluid density. The exit pressure is calculated using Equation 4.13.

$$P_{out} = \rho_{in} h + P_{in} \qquad \text{Equation 4.10}$$

The pump exit temperature is a function of the pump power, pump efficiency, mass flow rate, and average specific heat of the hydrogen flow. Equation 4.14 shows this relationship.

$$T_{out} = T_{in} + \frac{P_p \, \eta}{\dot{m} c_p} \qquad \text{Equation 4.11}$$

Since the results are based on the average specific heat, c_p, and iterative loop is used to converge the temperature-dependent specific heat. The initial operation point with known pump power and head are used to adjust the pump head for different pumping powers via the pump affinity laws. The pump efficiency is calculated using Equation 4.15. This function is executed at point 1 in Figure 3.8.

$$\eta = \frac{h}{P_p \dot{m}} \qquad \text{Equation 4.12}$$

The piping in the expander cycle is assumed to have zero heat generation and is adiabatically insulated from the surrounding components. The Kazmi friction factor

correlation is used in a simple pressure drop calculation across a single node. The pressure drop across the piping section can be model by Equation 4.16. This equation accounts for friction losses and acceleration losses in the fluid flow, losses due to gravity are assumed by zero in all the T/H calculations.

$$P_{out} = P_{in} - \frac{fl}{De_H \rho \, v^2/2} - (\rho_{in} v^2 - \rho_{out} v^2) \qquad \text{Equation 4.13}$$

Where f is the friction factor, l, is the length of the pipe, De_H is the hydraulic diameter, and v is the fluid velocity. This function is executed in-between point 1 and point 2 in Figure 3.8.

The nozzle coolant circuit and reflector flow channels are solved in a similar manner to the fuel element and moderator element flow paths, using the Kazmi friction factor correlation. The flow path geometry of the nozzle was tailored to match the exit conditions of the nozzle presented by previous research [31]. The geometry of the reflector flow path is based on the reflector coolant channel configuration using in previous NERVA KIWI designs [30]. The pressure drop through the nozzle and reflector is calculated using Equation 4.16. The nozzle and reflector length was divided into 30 axial nodes. The nozzle is assumed to have a uniform axial power profile, while the radial reflector was axially segmented and the power profile was obtained directly from Serpent. The increase in bulk coolant temperature was calculated using Equation 4.7. This function is executed in-between points 3r and 4r in Figure 3.8. The reflector function is executed in-between points 4r and 5r.

The mixing chamber function is used to mix the flow after exiting turbine, and at the junction between the reflector coolant circuit and the moderator coolant circuit. Each mixing chamber is assumed to be adiabatic. The recombined exit temperature of the mixing chamber is calculated using Equation 4.17. This function is executed at point 8 and after the turbine in Figure 3.8.

$$T_{out} = \frac{\dot{m}_1 c_{p,1} T_{in,1} + \dot{m}_2 c_{p,2} T_{in,2}}{\dot{m}_1 c_{p,1} + \dot{m}_2 c_{p,2}} \qquad \text{Equation 4.14}$$

In an expander cycle, the pump and turbine share the same shaft and therefore must have the same power, and shaft speed. The turbine is assumed to have a constant pressure ratio for all mass flow rates. The turbines remove energy from the hydrogen flow to provide power for the pumps. The outlet pressure is determined by the turbine's pressure ratio. The outlet temperature can be calculated using Equation 4.18 in an iterative loop to convergence on the temperature-averaged specific heat. This function is executed at point 7 in Figure 3.8.

$$T_{out} = T_{in} - \frac{P_p \, \eta}{\dot{m} c_p} \qquad \text{Equation 4.15}$$

The system mass, m_{sys}, can have significant effects on the thrust-to-weight ratio performance parameter of an NTP design. It is not possible to precisely analyze pump and turbine weights for a wide range of operating conditions, consequently dimensional analysis is used to determine the turbo-pump system mass. For geometrically similar pumps operating at a fixed maximum impeller tip speed, and therefore a given flow velocity, the gas handling capacity of any pump is proportional to the flow area of the

pump. Therefore, the area of the pump is proportional to some characteristic linear dimension D. The weight of the pump is proportional to the surface area of the pump times the wall thickness, and therefore to Dt^2. The structure thickness is proportional to the pump exit pressure and exit diameter. This correlation is represented by Equation 4.19, where Q_f is the volumetric flow rate and P_d is the pump discharge pressure. A similar dimensional analysis applies to the turbine and is presented in Equation 4.20.

$$m_{pump} \propto P_d Q_f^{3/2} \qquad \text{Equation 4.16}$$

$$m_{turbine} \propto \left(P_d Q_f\right)^{3/2} \qquad \text{Equation 4.17}$$

The weight of the piping in the expander cycle is a function of the volumetric flow rate, and pressure in the piping shown by Equation 4.21. L_p, δ, and v represent the length, wall density, and material tensile strength of the pipe.

$$m_{pipes} \propto \frac{2L_p}{\delta v} P_f Q_f \propto P_f Q_f \qquad \text{Equation 4.18}$$

These contributing factors are accounted for in the correlation presented in Equation 4.22. Where $C_1 = 1 \frac{\left[{}^{lb-s}/_{ft^3}\right]}{\left[{}^{lb}/_{in^2}\right]^{2/3}}$ and $C_2 = 100\ [lb]$, these constants are based on the ROVER program estimates of pumping plant masses and should provide conservative estimates of current rocket technology [39].

$$m_{sys} = C_1 Q_f P_d^{2/3} + C_2 \qquad \text{Equation 4.19}$$

4.4.3 POWER Validation

The functions in the POWER script were validated against published nuclear propulsion system simulation (NPSS) results for both large and small engine configurations [31]. It is important to note that the hydrogen material properties libraries used might be slightly different than the ones used with NPSS; therefore, small differences between POWER and NPSS are expected. Table 4.1 compares results for a large NERVA system and Table 4.2 compares a small ANL system. There agreement between POWER and NPSS results is excellent.

Table 4.1 POWER large NEVRA sub-function vs NPSS

	Tin [K]	**Pin [MPa]**	$\dot{m}$ **[kg/s]**	**Tout [K]**	**Tout [K]**	**Pout [MPa]**	**Pout [MPa]**
Function				*NPSS*	*POWER*	*NPSS*	*POWER*
Pump	22.00	0.22	6.34	38.00	40.96	15.65	15.66
Turbine	387.00	13.61	3.86	353.00	351.00	8.38	8.38
Mixing Chamber	387.00, 353.00	13.61, 8.38	2.48, 3.86	367.00	366.00	8.38	8.38
Nozzle	39.00	15.35	7.53	171.00	172.00	14.29	14.29
Reflector	171.00	14.29	7.53	260.00	259.00	13.61	13.62

Table 4.2 POWER small NEVRA sub-function vs NPSS

	Tin [K]	**Pin [MPa]**	$\dot{m}$ **[kg/s]**	**Tout [K]**	**Tout [K]**	**Pout [MPa]**	**Pout [MPa]**
Function				*NPSS*	*POWER*	*NPSS*	*POWER*
Pump	21.00	0.22	3.76	34.00	33.21	9.53	9.53
Turbine	254.00	8.01	2.39	232.00	231.19	4.81	4.81
Mixing Chamber	232, 254	4.81, 8.01	2.39, 0.04	144.00	145.33	4.81	4.81
Nozzle	35.00	9.23	2.34	144.00	145.33	8.37	8.37
Reflector	144.00	8.37	2.34	233.00	233.78	8.01	8.01

4.5 Thermal Properties

This section presents the temperature-dependent thermal conductivities for various materials used in this thesis. A study [40] on estimating thermal conductivity of cermet fuel materials found that a reasonable mean value fit for tungsten represented by the relations presented in Equation 4.20

$$k_W\left[\frac{W}{m\,K}\right] = \begin{cases} 165.54 - 85.57 \times \left(\frac{T}{10^3}\right) + 33.51 \times \left(\frac{T}{10^3}\right)^2 & T < 890 \\ 133.82 - 15.57 \times \left(\frac{T}{10^3}\right) & T \geq 890 \end{cases} \quad \text{Equation 4.20}$$

Work conducted at the NASA Lewis Research Center included the development of molybdenum-tungsten based cermet fuel materials [41]. Part of this research included the evaluation of the thermal conductivity of the molybdenum, presented in Equation 4.21.

$$k_{Mo}\left[\frac{W}{m\,k}\right]=\begin{cases}16.186T-0.00298T^3-0.0605T^2-4.545 & T<50\\ 0.02T^2-5.4776T+522.44 & 50\le T<150\\ 9\times10^{-6}T^2-0.0513T+153.29 & T\ge150\end{cases}$$ Equation 4.21

There is currently no readily available thermal conductivity data above 1910 K for UN. In order to provide a conservative estimate at higher temperatures the thermal conductivity of UN is assumed to be constant above 1910 K [42].

$$k_{UN}\left[\frac{W}{m\,K}\right]=\begin{cases}1.43T^{0.39} & T<1910\\ 27 & T\ge1910\end{cases}$$ Equation 4.22

There are three basic models: series, parallel, and geometric mean models to calculate thermal conductivity of a material formed from one or more discrete components imbedded in a homogenous, continuous, stationary medium [43]. The most conservative of the three models is the parallel model presented in Equation 4.23.

$$k_{matrix}\left[\frac{W}{m\,k}\right]=\frac{1-wt\%_j}{k_i}+\frac{wt\%_j}{k_j}$$ Equation 4.23

Where k_i and k_j are the thermal conductivities of components *i* and *j*, and $wt\%_j$ is the weight fraction of the component *j*.

In order to account for the addition of the uranium fuel kernels to the matrix material the Bruggerman method [44] was utilized and is presented in Equation 4.24.

$$k_{fuel}\left[\frac{W}{m\,k}\right] = k_{kernel} + \left(1 - V_p\right) \times \left(k_{matrix} - k_{kernel}\right) \times \left(\frac{k_{kernel}}{k_{matrix}}\right)^{1/3} \quad \text{Equation 4.24}$$

In order to reduce the heat load in the moderating element, a 70% porous ZrC material was used. This insulating material was developed at Los Alamos and the conductivity data are presented in Equation 4.28 and were retrieved from the technical report produced by Los Alamos. The conductivity of this material is less than 1 W/m K at room temperature compared to a 50 W/m K for a typical non-porous ZrC material.

$$k_{ZrC}\left[\frac{W}{m\,k}\right] = 0.5209 + 9.812 \times 10^{-4}T + 1.045 \times 10^{-7}T^2 \quad \text{Equation 4.25}$$

The conductivity of Zircaloy, presented in Equation 4.25, was adopted from the materials for light water reactors database [45], which is valid in the temperature range from 300 to 1800 K.

$$k_Z\left[\frac{W}{m\,k}\right] = 131.2 - 0.08432T + 1.96 \times 10^{-5}T^2 \quad \text{Equation 4.26}$$

The thermal conductivity of zirconium hydride is not significantly affected by the temperature and shows nearly constant value of 16–18 W/m K. Therefore, it was decided to adopt the value of 16 W/m K. The thermal conductivity for the graphite is presented [46] in Equation 4.26.

$$k_C\left[\frac{W}{m\,k}\right] = 131.2 - 0.08432T + 1.96 \times 10^{-5}T^2 \quad \text{Equation 4.27}$$

4.6 Nozzle Performance Calculator

The rocket performance is measured based on the thrust and I_{sp} delivered. To evaluate the chamber conditions this thesis adopts the method developed by Sutton and Biblarz [47]. The code relies on overall system and core T/H analysis to provide the chamber temperature, chamber pressure, mass flow rate, and nozzle expansion ratio. Figure 4.8 displays the considered convergent-divergent nozzle schematic. An expansion ratio of 300 was used for all nozzle calculations presented in this thesis.

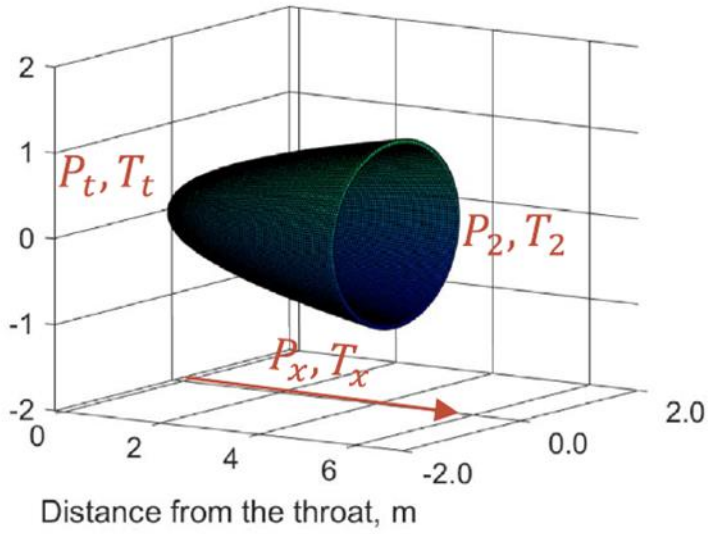

Figure 4.8 Convergent-Divergent Nozzle [48]

The calculation of the nozzle begins by iteratively calculating the throat conditions. Where P_t is the throat pressure and T_t is the throat temperature. The throat pressure is calculated via Equation 4.28, while the throat temperature is calculated using Equation 4.29.

$$P_t = P_1\left(\frac{2}{k+1}\right)^{\frac{k}{k-1}}$$ Equation 4.28

$$k = \frac{c_p}{c_v}$$

$$V_t = V_1\left(\frac{k+1}{2}\right)^{\frac{k}{k-1}}$$ Equation 4.29

$$T_t = \frac{2T_1}{k+1}$$

Once the throat pressure and temperature have been obtained, the critical throat velocity can be calculated using Equation 4.30.

$$v_t = \sqrt{\frac{2k}{(k+1)}RT_1}$$ Equation 4.30

In the divergent portion of the nozzle the gas expands which results in a decrease in pressure and increase in velocity to super-sonic conditions. For a supersonic nozzle, the ratio between the throat and any internal nozzle area with a pressure of P_x can be determined via Equation 4.31.

$$\frac{A_t}{A_x} = \left(\frac{k+1}{a}\right)^{\frac{1}{k-1}}\left(\frac{P_x}{P_1}\right)^{\frac{1}{k}}\sqrt{\frac{k+1}{k-1}\left[1-\left(\frac{P_x}{P_1}\right)^{\frac{k-1}{k}}\right]}$$ Equation 4.31

This area ratio is already known along the length of nozzle since the expansion ratio is given. If the specific heats are known, then the pressure P_x can be calculated. This value is then used to calculate the temperature T_x along the nozzle, via Equation 4.32.

$$T_x = T_t \left(\frac{P_x}{P_1}\right)^{\frac{k-1}{k}} \qquad \text{Equation 4.32}$$

The thrust and specific impulse is evaluated using the nozzle exit velocity, which is calculated using Equation 4.33.

$$\frac{v_x}{v_t} = \sqrt{\frac{k+1}{k-1}\left[1 - \left(\frac{P_x}{P_1}\right)^{\frac{k-1}{k}}\right]} \qquad \text{Equation 4.33}$$

The nozzle calculator uses discretized, multiple 1D, regions to account for the change in hydrogen properties. The ratio of specific heats, k, is a function of the gas temperature and pressure, which is rapidly changing inside the nozzle. An iterative solution method was implemented to update the gas properties. The thrust provided by the nozzle is calculated via Equation 4.34, where $\dot{m}$ is the mass flow rate, P_2 is the nozzle exit pressure, and P_3 is zero because the rocket is operating in a vacuum.

$$F = \dot{m}v_2 + (P_2 - P_3)A_2 \qquad \text{Equation 4.34}$$

The I_{sp} is calculated via Equation 4.35, where g_o is the standard acceleration due to gravity.

$$I_{sp} = \frac{v_2}{g_o} + \frac{P_2 A_2}{\dot{m} g_o}$$ Equation 4.35

CHAPTER 5. SENSTIVITY STUDIES

This chapter presents sensitivity studies performed to determine the effect of the axial split ratio, inlet fuel temperature, radial peaking factor, and target Mach number on engine performance. The axial power profiles were calculated directly from the Serpent neutronics model, 90 nodes were used in the thermal hydraulic solutions of the moderator and fuel elements to capture the gradients in thermal properties.

5.1 Axial Power Profile Sensitivity

In this section, the analyses were conducted for axial splits of 0.3, 0.6, 0.7, and 0.9 using a fixed ME:FE ratio of 2.14, and moderator flow fraction of 0.5, target Mach number of 0.1, target chamber pressure of 6.89 MPa, and a radial peaking factor of 1.2. The fuel elements power density profiles are presented in Figure 5.1 and moderator element power density profiles are presented in Figure 5.2. The area (i.e., total power) under each curve is not the same for each examined case, but rather the maximum allowable reactor power for each configuration was obtained by the iterative methodology implemented in the POWER script. The highest split ratio cores can withstand a higher total reactor power due to the increased melting temperature of tungsten. This is also the reason why the 0.9 split fuel achieves the highest fuel element exit temperature.

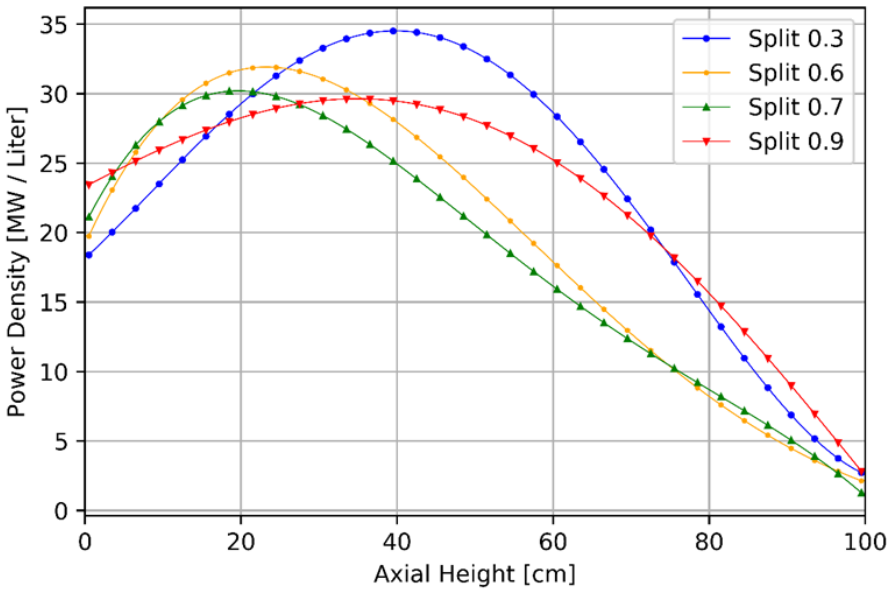

Figure 5.1 Fuel Element Power Density Profile

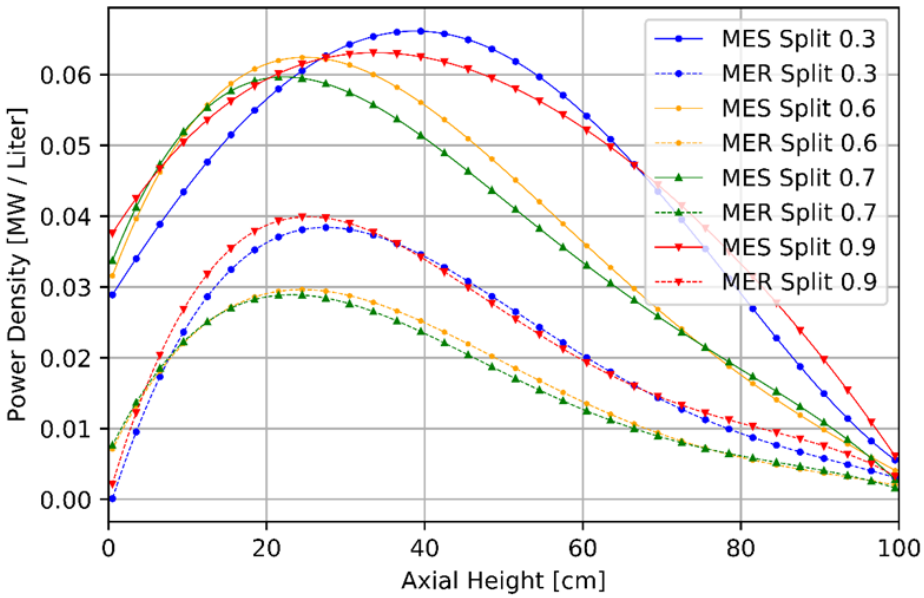

Figure 5.2 Moderator Element Supply and Return Power Density Profiles

The power distribution is not a monotonic function of the axial split as both the fuel temperature, which changes by above 2000 K from inlet to outlet, and the propellant density determine the power shape. However, the general trend for most cases demonstrate that for lower axial split values, the power is drawn towards the upper part of the core where the propellant enters the fuel channels. This is the result of the lower absorption cross-section of the molybdenum, which increases the local reactivity of these regions. Figure 5.3 shows that the 0.7 split case has the strongest initial peaking of almost 1.2 at the entrance. As will be shown later, the power density near the propellant entrance with molybdenum as the fuel matrix must be constrained, otherwise it will reach its thermal failure. This is primarily a result of the degraded heat transfer mechanism as the propellant flow is not fully developed. This potential caveat will be discussed in details in section 5.2.

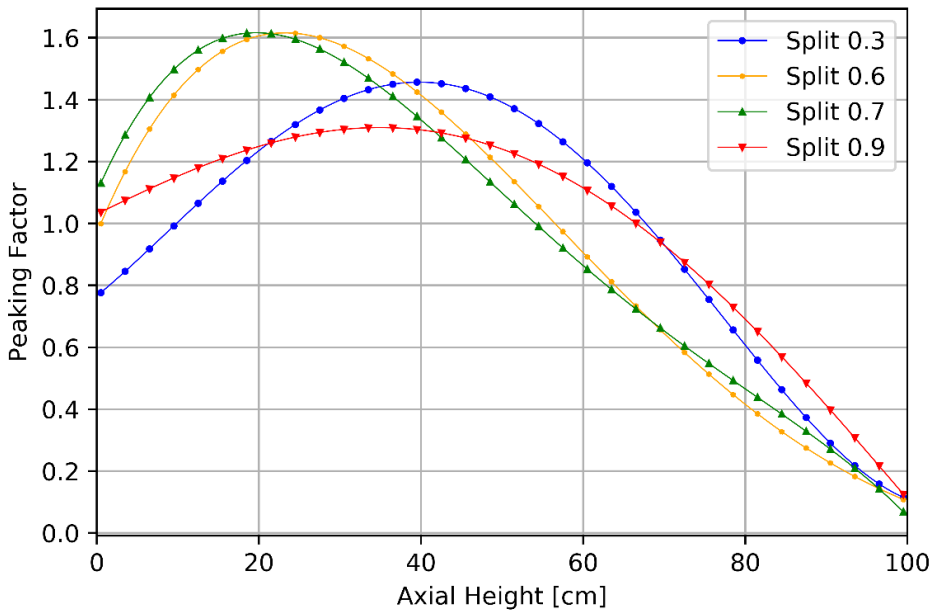

Figure 5.3 Normalized Fuel Element Power Profile

The bulk hydrogen temperature distributions for the average moderator supply, moderator return, and fuel element channels are presented in Figure 5.4. The 0.9 split case has the highest exit hydrogen temperature due to the increased total reactor power. The centerline fuel temperature is presented in Figure 5.5. The moderator supply and return hydrogen temperatures are shown to be continuous; however, there is a discontinuity between the moderator return exit temperature and fuel element inlet temperature. This difference is caused by the mixing of the moderator return flow with the flow from the radial reflector, which then passes through the turbine before entering the fuel element. The hydrogen flow loses energy passing through the turbine, which decreases the temperature of the gas entering the fuel element. The inlet temperature to the fuel element channels can have a significant effect on the I_{sp} of the engine. This effect will be detailed in section 5.2.

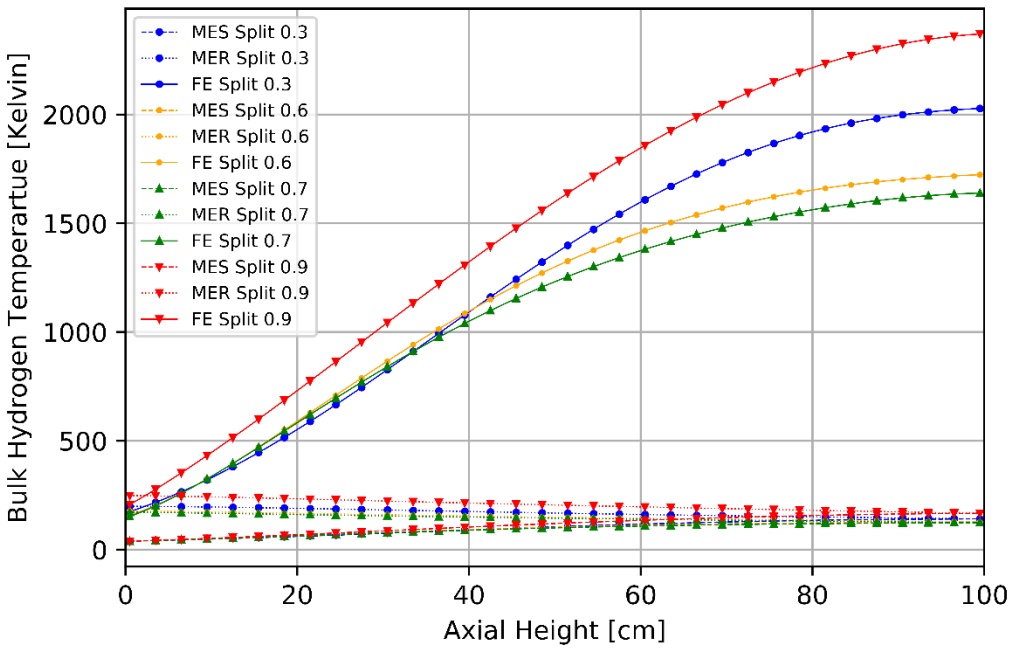

Figure 5.4 Bulk Hydrogen Temperature Profiles

The highest exit bulk hydrogen temperature of 2420 K was achieved with an axial split of 0.9. Higher split ratio cores have a higher maximum power limit than lower split height cores if the location of the limiting node is located in the molybdenum-tungsten mixture matrix material, which has an increased allowable centerline fuel temperature compared to the molybdenum matrix.

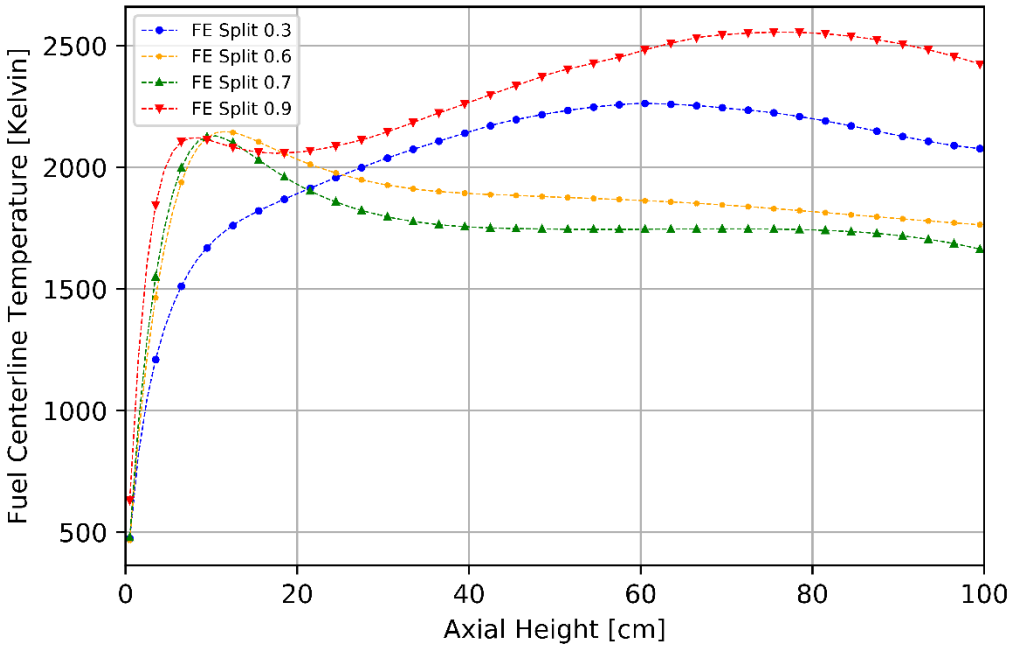

Figure 5.5 Fuel Centerline Temperature Profiles

The coolant outlet temperature of each design is highly dependent on the shape of the centerline fuel temperature and the temperature capability of the limiting node. The 0.9 axial split case allows the centerline fuel temperature to be higher in the initial nodes of fuel element; thus allowing to operate at higher overall power and consequently obtain the highest coolant exit temperatures. To conclude, the centerline fuel temperature profile can

limit the total power level of the reactor if the power is shifted closer to the regions with only molybdenum, this effect is displayed in the 0.6 and 0.7 split cases.

5.2 Fuel Element Inlet Temperature Sensitivity

One of the major advantages of the developed computational framework is the ability to study the impact of various boundary conditions, such as the inlet temperature conditions to the fuel element. The fuel element power, geometry, mass flow rate, inlet pressure, and power profile were fixed for the results presented in this section. The only variable perturbed was the inlet fuel temperature. The case chosen for this sensitivity study has a moderator to fuel element ratio of 2.14 and an axial split of 0.7. This axial split ratio was chosen because the I_{sp} of the 0.7 axial split ratio cores were observed to be strongly affected by the fuel element inlet temperature. This effect has two major drivers, the first is the shape of the axial power profile, and the second is the heat transfer coefficient. Designs with an axial split of 0.7 have power peaks near the entrance of the fuel element, this peaking results in relatively high fuel element surface temperatures when compared to the bulk coolant temperature. The Taylor heat transfer correlation, shown in Equation 4.6, relies on a correction term which takes into account the ratio of the wall surface temperature and bulk coolant temperature. The effect of the inlet temperature on the fuel centerline temperature is presented in Figure 5.6. As the inlet temperature increases the centerline temperature peak decreases, only the first 40 centimeters of the flow channel is presented since the centerline fuel temperature remains fairly constant after. The reduction in the centerline fuel temperature peak is caused by the increase in the heat transfer coefficient as the inlet fuel temperature increases. Figure 5.6 shows the significant advantage of increasing the inlet fuel temperature. By increasing the inlet temperature, the limiting node

is moved back to approximately 20 centimeters (towards the tungsten regions), which would allow for the total power of core to be increased resulting in a much higher exit fuel temperature. The maximum centerline temperature for each case is plotted as a horizontal line, by increasing the inlet temperature from 173 kelvin to 313 kelvin the maximum centerline temperature in the average channel decreased from 2163 kelvin to 1984 kelvin. However, the minimum centerline temperature of 1966 kelvin occurred with an inlet temperature of 293 kelvin. This suggests that there may be an optimal inlet temperature for each axial power shape, which could maximize the power density of each fuel element.

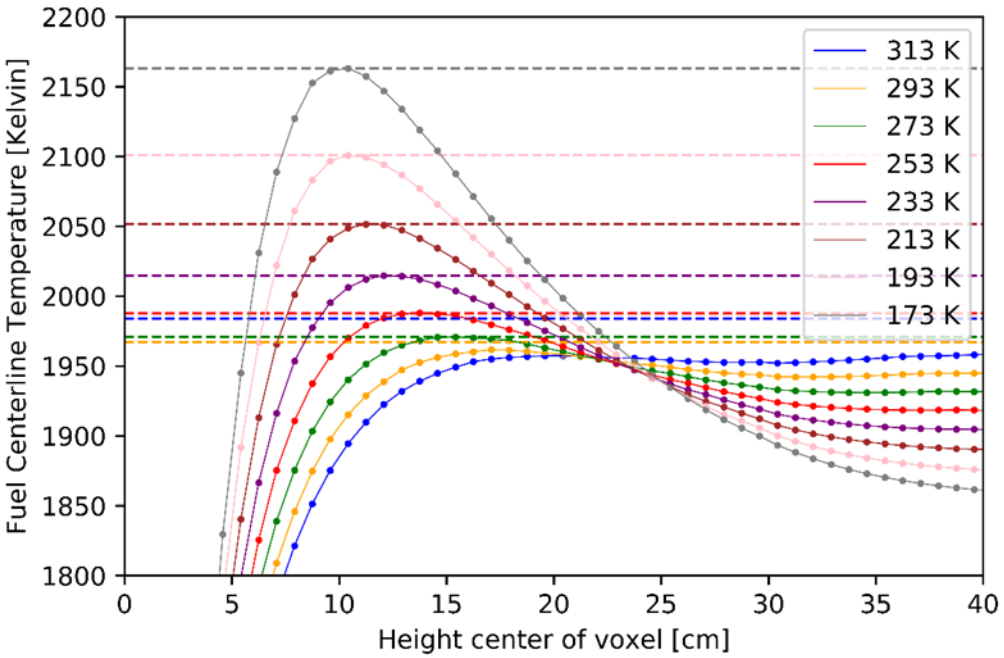

Figure 5.6 Fuel Centerline Temperature Sensitivity to Inlet Temperature

The initial centerline fuel temperature spike displayed in Figure 5.6 is caused by the heat transfer coefficient reaching its minimum in first 10 centimeters of the flow channel. This trend is presented in Figure 5.7. The Prandtl number and thermal conductivity are not

presented due to the fact that they remain almost constant through the flow channel. The ratio of the surface wall temperature to the bulk coolant temperature is shown in Figure 5.8, the shape function $-0.57 - 1.59 * D/X$ is shown in Figure 5.9, and the Reynolds number is shown in Figure 5.10. The shape function is identical for all cases since it is only dependent upon the geometry, which is the same for all cases presented in this study. The Reynolds number is always decreasing, which has a positive impact on the heat transfer coefficient. As the inlet temperature increases the ratio of surface wall temperature to bulk coolant temperature decreases which causes the heat transfer coefficient to increase. The temperature ratio term in the Nusselt number correlation is used to account for the fact the temperature profile in the gas is not fully established even for large x/D values [50]. Figure 5.6 and Figure 5.7 demonstrate that the overall performance of the engine would benefit from higher inlet fuel temperatures.

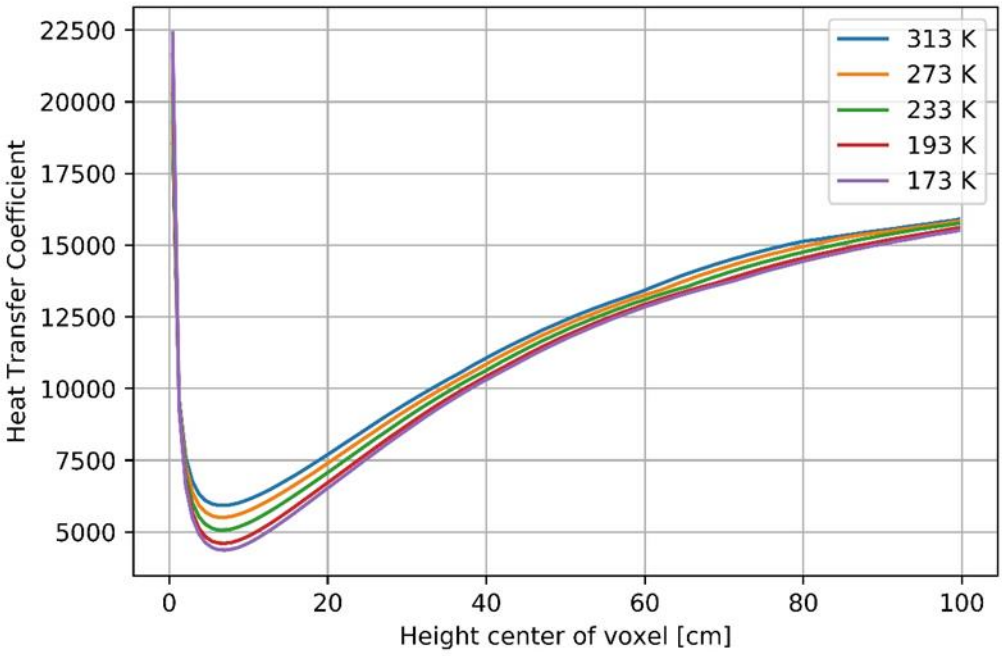

Figure 5.7 Heat Transfer Coefficient Sensitivity to Inlet Temperature

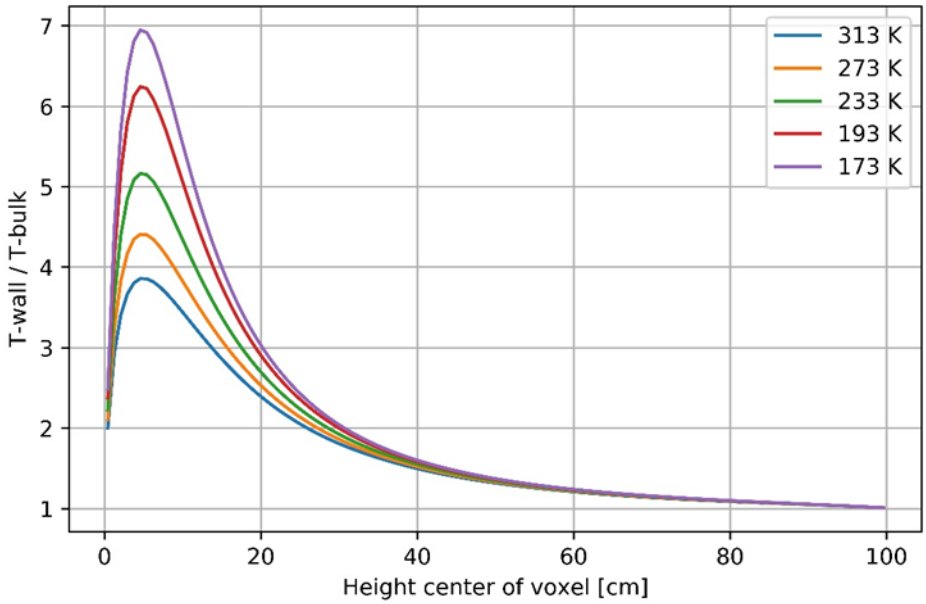

Figure 5.8 Wall Temperature to Bulk Coolant Temperature Ratio Sensitivity to Inlet Temperature

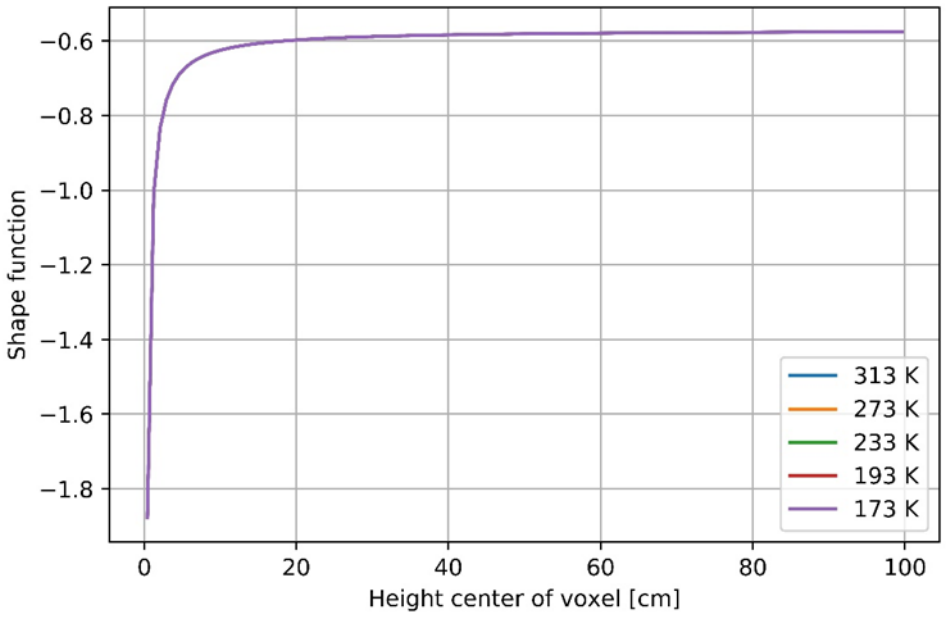

Figure 5.9 Shape Function Sensitivity to Inlet Temperature

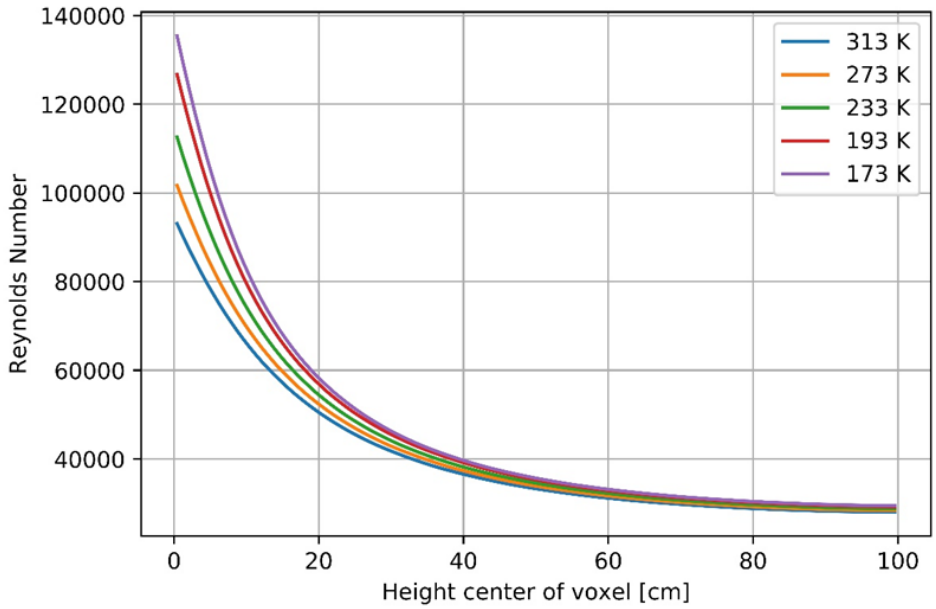

Figure 5.10 Reynolds Number Sensitivity to Inlet Temperature

5.3 Radial Power Peaking Sensitivity

The radial peaking factor of the reactor can have significant impacts on the I_{sp} of the engine. The radial peaking factor determines how severely the hot channel in the reactor will limit the maximum allowable power. This study considers cores with an ME:FE ratio of 1.96, a target Mach number of 0.1, moderator flow fraction of 0.5, and a target chamber pressure of 6.89. Figure 5.11 compares radial peaking factors of 1.2 and 1.05. Reduction of the radial peaking factor can be achieved by radial zoning of uranium enrichment, or by optimization of the core pattern arrangement. This task is outside the scope of this thesis, however future studies should consider this optimization. A significant increase of approximately 50 seconds of I_{sp} can be achieved if the radial peaking factor is reduced to 1.05.

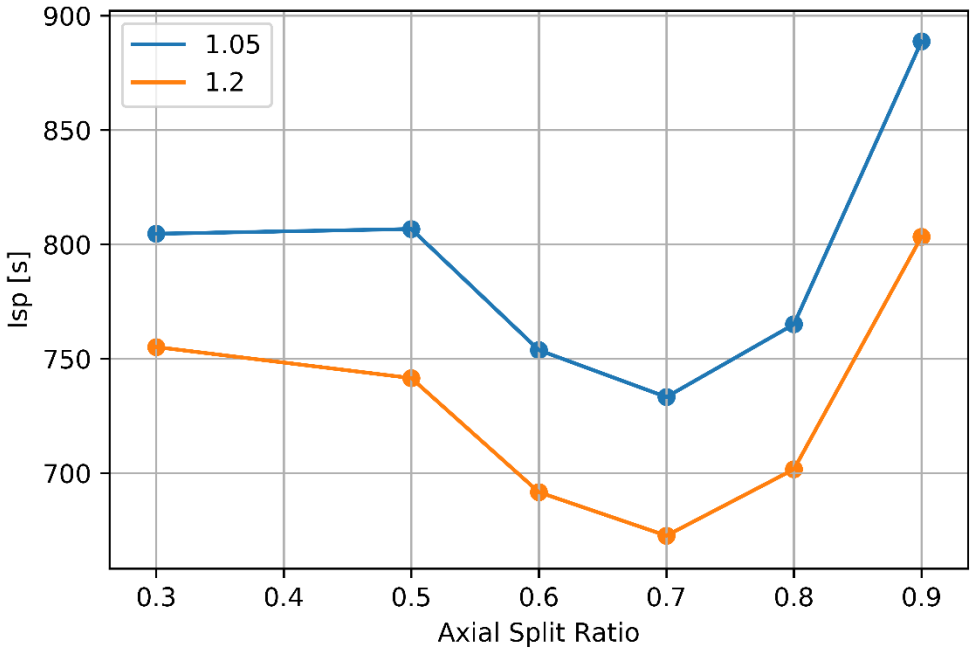

Figure 5.11 I_{sp} sensitivity to radial power peaking

5.4 Target Mach Number Sensitivity

The target Mach number has a strong impact on the mass flow rate, and therefore the thrust of each engine. This study considers cores with an ME:FE ratio of 1.42, a radial peaking factor of 1.05, moderator flow fraction of 0.5, and several axial split ratios. Figure 5.12 shows a clear separation between each of the target Mach numbers. Higher target Mach numbers can achieve greater thrust but reduced I_{sp} performance. The dashed red lines in Figure 5.12 show the 25 klb_f thrust and 875 I_{sp} isolines. The only target Mach number that has a case that meets both the I_{sp} and Thrust requirements is 0.1, therefore the design

space analysis will consider cases targeting a Mach number of 0.1. In addition, this target Mach results in mass flow rates compatible with existing turbo-machinery capabilities.

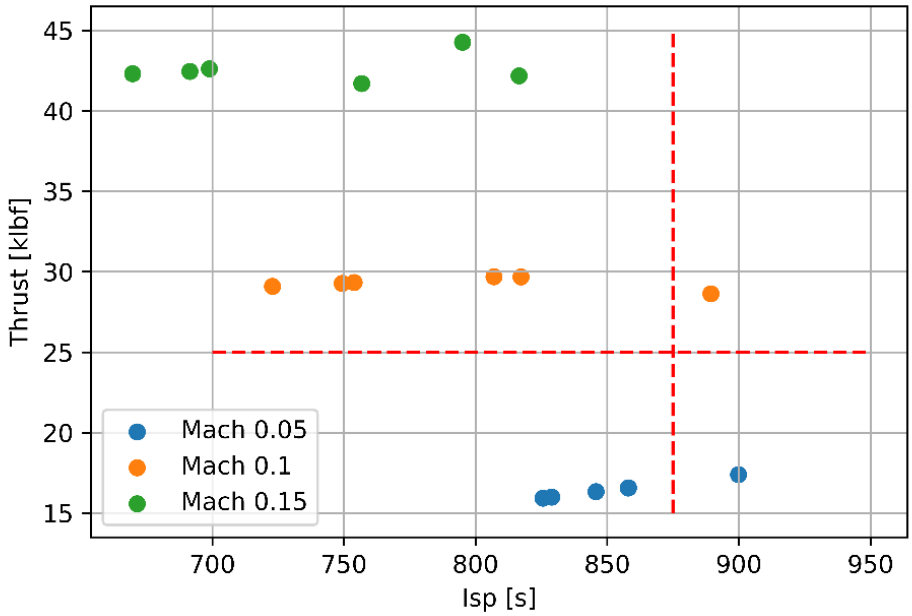

Figure 5.12 Thrust and I_{sp} sensitivity to target Mach number

CHAPTER 6 DESIGN SPACE ANALYSIS

The NTP design space was mapped for more than 2400 unique cores each with a unique ME:FE ratio and axial split ratio. For each individual case, the fuel, moderator and reflector power profiles were obtained using Serpent. All cases within the design space target a nozzle chamber pressure of 6.89 MPa, moderator flow fraction of 0.5, an exit Mach number of 0.1, a nozzle expansion ratio of 300. The target pressure value aligns with previous analysis performed by NASA Glenn Research Center on NTP's of a similar size

and power level targeted a chamber pressure of 6.89 MPa [31]. The KIWI-4B cold flow testing discovered that NTP systems with Mach number exceeding 0.3 were subject to flow instabilities, and mechanical harmonic oscillations caused serious damage to elements inside the core during the testing campaign [1]. Therefore, a healthy margin was left in the design space to account for future design optimizations that would increase the exit Mach number, such as flow orifficing and core geometry configuration. Additionally, targeting a Mach number of 0.1 forces total system mass flow to remain under the maximum flow rate a RL-60 dual-pump system can accommodate.

6.1 Design Space Mapping

LEU NTP cores rely on relatively compact designs, which are almost always under-moderated systems and thus the results shown in Figure 6.1 are somewhat intuitive. As the moderator to fuel element ratio increases, k_{eff} increases as well. Additionally, as the split ratio decreases the amount of tungsten in the core is also reduced. The latter results in increasing k_{eff} since the tungsten neutron absorption cross-section is significantly larger than that of molybdenum. In Figure 6.1 the yellow to red region represents sub-critical cores. The white line shows where the transition from sub-critical to critical and super critical cores contained in the blue region. This line shows that as the split ratio increases the required number of moderator elements rapidly increases. The design space presented in subsequent analysis will only contain ME:FE ratios above 1.06 because cores with an ME:FE ratio less than 1.06 are deeply sub-critical.

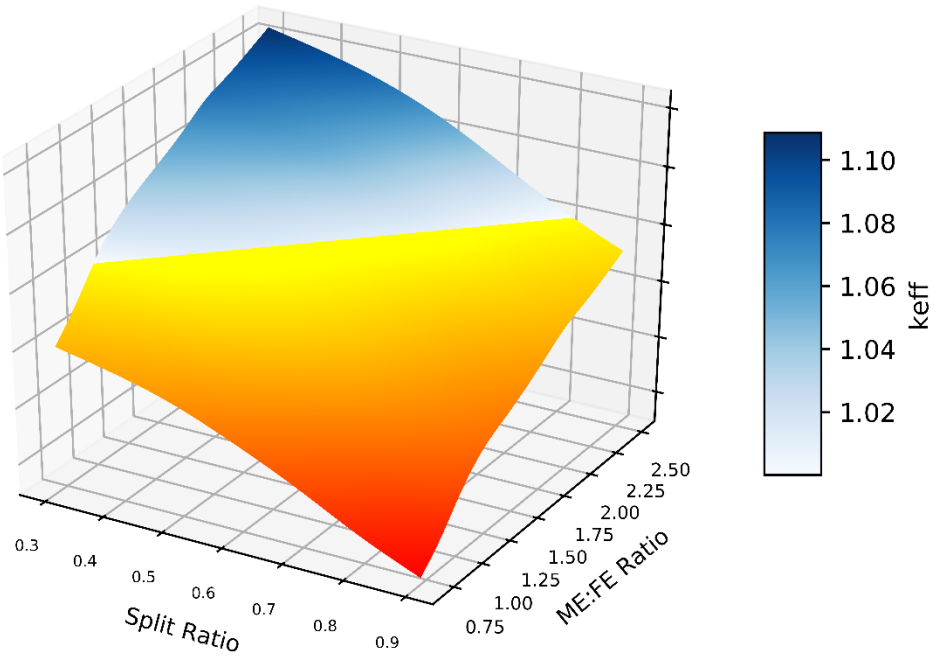

Figure 6.1 k_{eff} Design Space Map

The thrust produced by a rocket engine is heavily dependent upon the nozzle expansion ratio, nozzle inlet pressure, and mass flow rate entering the nozzle. In this study, a nozzle expansion ratio of 300, and a chamber pressure of 6.89 MPa were fixed for all the examined cases. The thrust as a function of split-ratio and ME:FE-ratio is shown in Figure 6.2. The mass flow rate for each case was determined by iterating on the maximum allowable fuel temperature while constraining the Mach number to 0.1. The total power of the system is higher for configurations having more fuel elements, *i.e.* lower ME:FE ratio. Larger number of fuel elements also translates to higher mass flow rates, which subsequently lead to increased thrust values. It must be mentioned that the split ratio affects the axial power distribution, which in turn varies the pressure drop; however, this is a second order effect and thus thrust is split ratio invariant. By constraining the exit Mach number of the system,

which is a function of the pressure and temperature of the gas, the outlet velocity of the gas is fixed. The result of this constraint is that the mass flow rate per fuel channel is almost constant across all of the cases. This explains why the thrust is a weak function of the axial split.

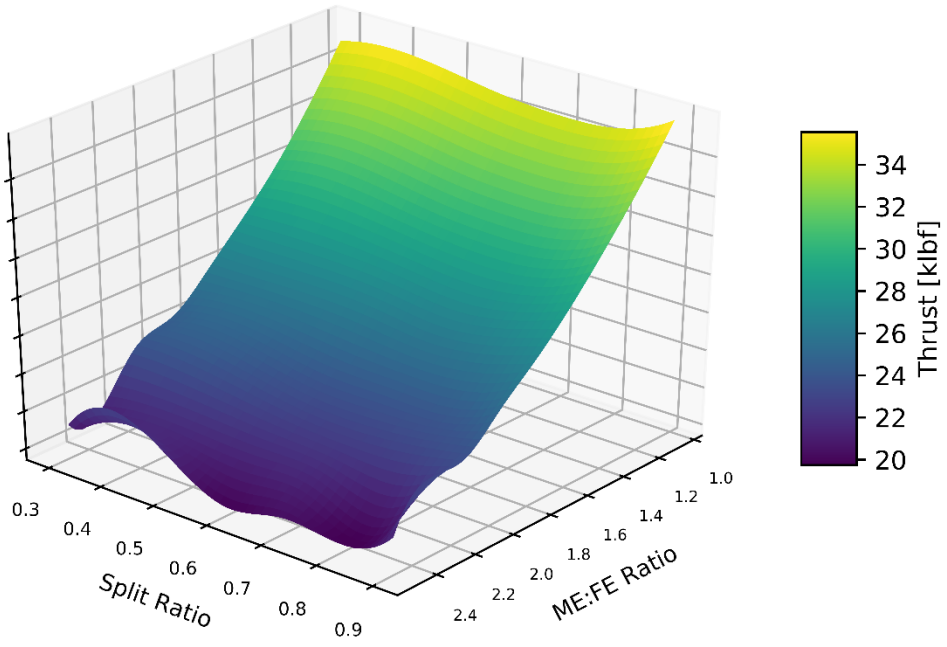

Figure 6.2 Thrust Design Space Map

There are two competing components of the engine mass: the reactor core mass and the turbo-pump machinery mass. The reactor mass, presented in Figure 6.3, is a function of the ME:FE ratio and axial split. The number of elements and reactor height in the design space is fixed. Therefore, as the number of fuel elements replaced by moderator elements increases, the total reactor core mass decreases due to the moderator elements being significantly less dense than the fuel elements. Additionally, as the split ratio increases the density of the fuel element increases due to the increased tungsten loading in the core.

Figure 6.3 demonstrates that the reactor mass is more sensitivity to the ME:FE ratio than the axial split ratio. The mass of the turbo pump machinery is calculated based on the system volumetric flow rate and pump pressure. Equation 4.22 is dominated by the mass flow rate term, which forces the total engine mass trend to follow the total system mass flow rate trend. The total reactor and turbo-pump masses are taken into consideration when calculating the thrust-to-weight ratio, presented in Figure 6.5, for each configuration.

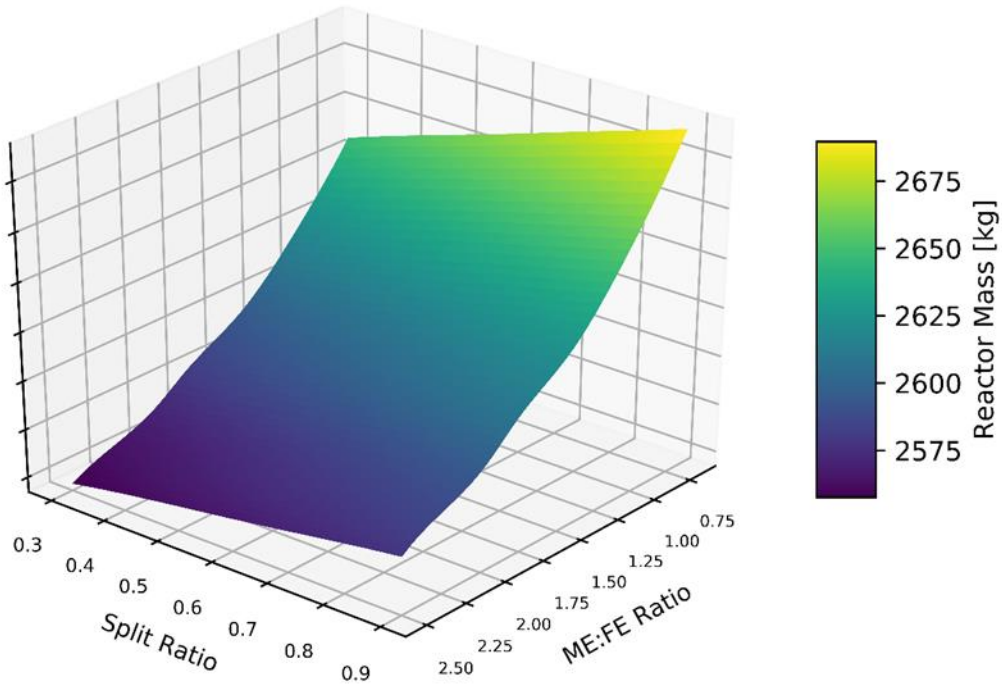

Figure 6.3 Reactor Mass Design Space Map

The total engine mass, presented in Figure 6.4, varies from approximately 6600 pounds to 7600 pounds. This shows that the majority of the engine mass is contributed from the reactor core. While reducing the mass of the turbo-pump system will be beneficial for

rocket performance, the majority of the weight reduced should be focused on the reactor core.

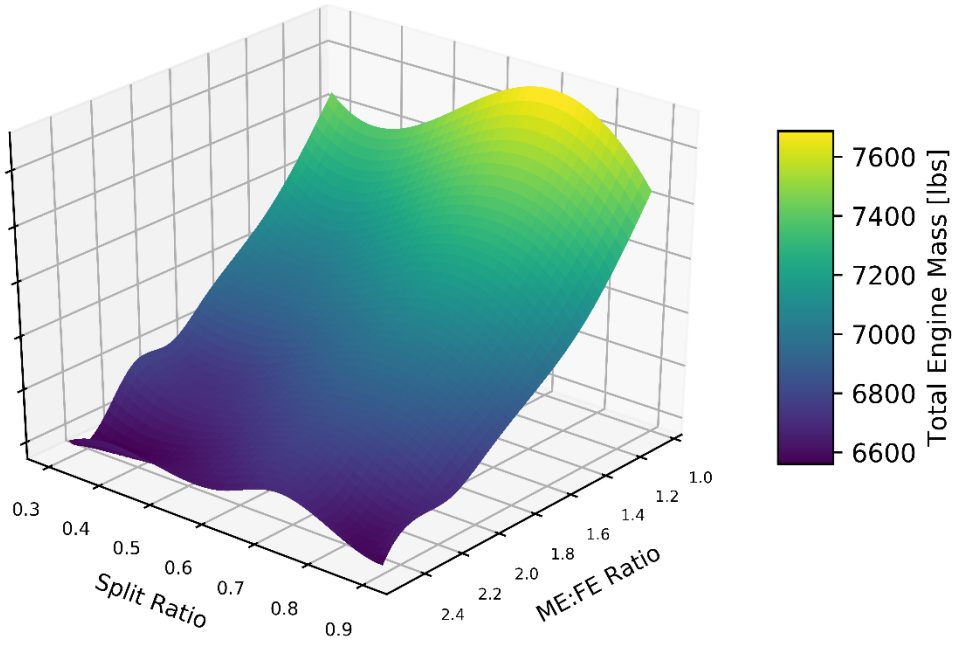

Figure 6.4 Engine Mass Design Space Map

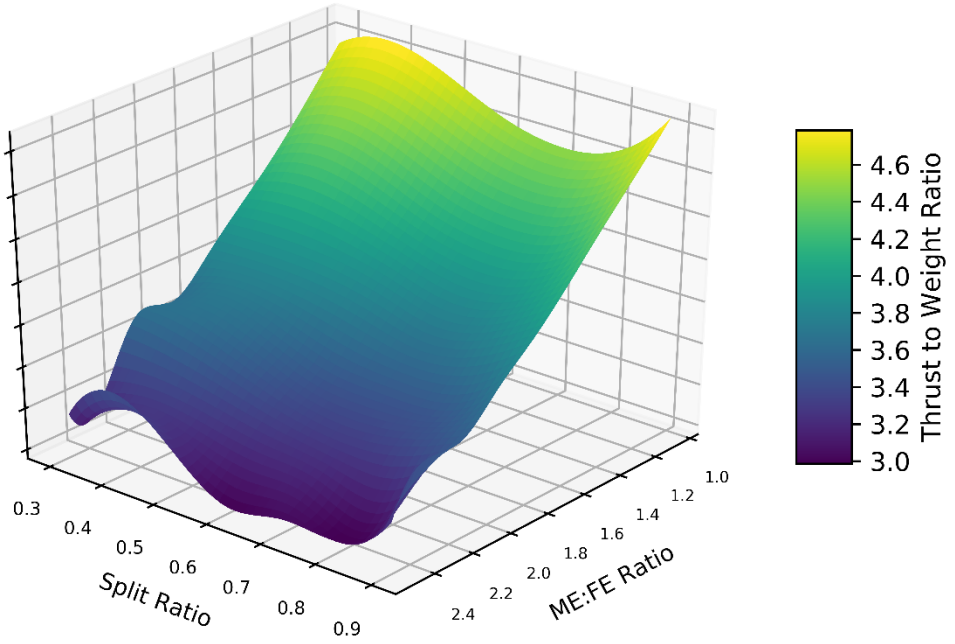

Figure 6.5 Thrust to Weight Ratio Design Space Map

One of the unconstrained parameters of the design space evaluation is the I_{sp}. As a matter of fact, the specific impulse should only be treated as the objective function to be maximized while satisfying all the constraints. If, however, the specific impulse is treated as a constraint thus adopting fixed chamber temperature, the POWER script iteration loop may force some of the designs to exceed the maximum allowable centerline fuel temperature, therefore forcing the design to fail. The approach taken by this thesis demonstrates the performance envelop of a fixed exterior dimension design. Figure 6.6 presents the I_{sp} design space. The total power and hence the outlet temperature for each case is a function of the axial split ratio, axial power profile, and inlet fuel temperature. All of these competing effects results in the unique behavior of the I_{sp}, as shown in Figure 6.6. Two major observations can be deducted from Figure 6.6. Core configurations with very

high split ratios allow to achieve higher thermal performance and thus higher I_{sp} values. However, these cores are very heavy and subcritical. Fortunately, additional non-intuitive optimum split exists near the 0.4 value. These core configurations are considerably lighter and have sufficient reactivity margin to sustain the core critical for the mission duration. This set of solutions is achievable since the power distribution flattens and the power peaking values at the entrance are greatly reduced. For these cases, molybdenum exhibits considerably lower temperatures and the limiting axial layer in terms of thermal failure is driven away to regions populated with tungsten. As Tungsten has a much higher melting point, the power could be increased until the full potential of this high-temperature material could be exploited leading to an improved I_{sp}.

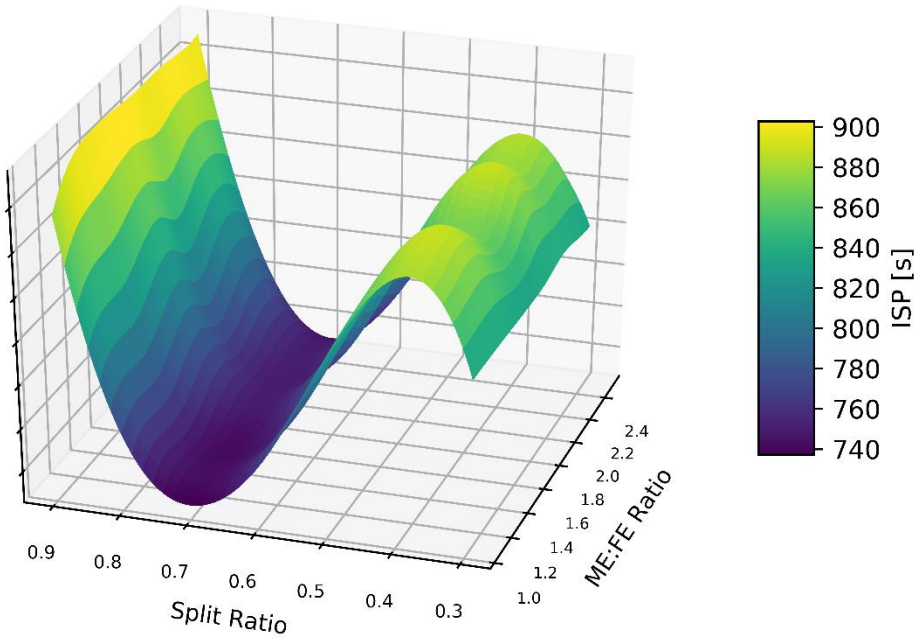

Figure 6.6 I_{sp} Design Space Map

As previously demonstrated the inlet temperature to the fuel elements, presented in Figure 6.7, affects the maximum attainable fuel temperature profile. By increasing the inlet temperature to the fuel elements, not only does the exit temperature increase, but the surface to wall temperature ratio decreases allowing for better heat transfer in the initial nodes. Increased heat transfer in the initial nodes can move the location of the limiting node deeper into the fuel regions having tungsten as the matrix material. It can be observed that inlet fuel element temperature has two maxima at split ratios of 0.9 and 0.4. The fuel element inlet shape mirrors the shape of the I_{sp} performance curve. The inlet temperature for 0.7 split cases is approximately 170 Kelvin, which based on the results presented in Figure 5.6 can cause significant fuel temperature peaking in the initial nodes.

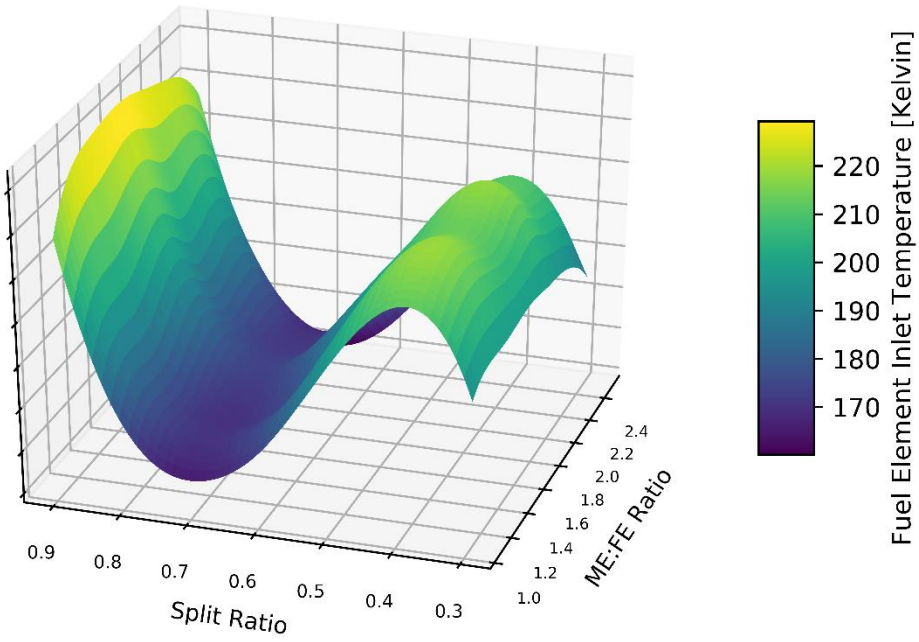

Figure 6.7 Fuel Inlet Temperature Design Space Map

Figure 6.8 presents the location of the limiting thermal node in the analyzed design space, where a height of zero represents the entrance to the fuel element. This figure confirms that the limiting node for axial split of 0.7 is near the entrance of the fuel element (*i.e.*, molybdenum). Once again peaks emerge at split ratios of 0.9 and 0.4 showing that the 0.9 and 0.4 cases are utilizing the high temperature material. The results demonstrate the I_{sp}'s complex dependence on the axial power shape, maximum allowable centerline temperature determined by the split ratio, and inlet conditions. More importantly, these results emphasize the need to perform further sensitivity and studies and quantify the associated uncertainties.

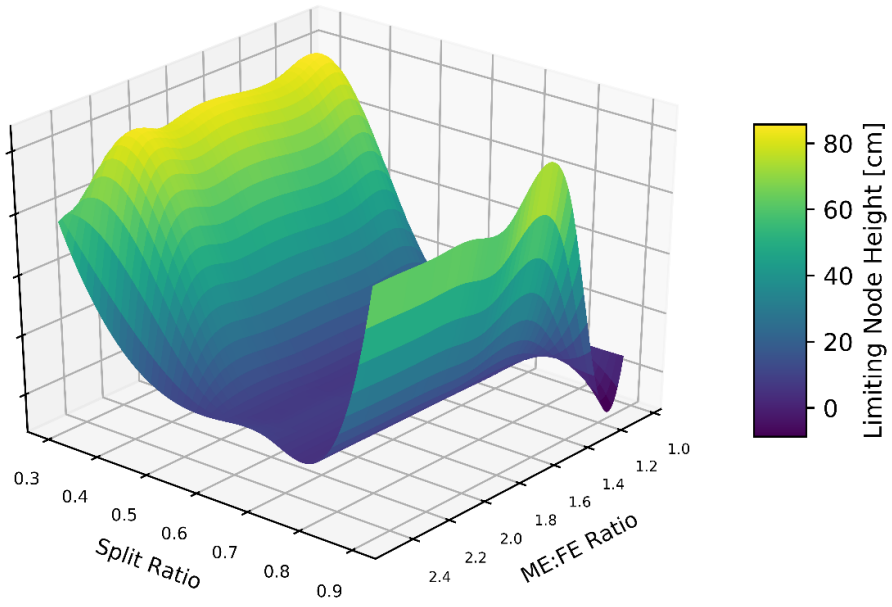

Figure 6.8 Limiting Node Height Design Space Map

6.2 Ideal Space Identification

NASA's Mars Design Reference Architecture 5.0 requirements have been summarized in Table 6.1. These specifications have been used to filter the design space and identify the optimal design region based on the minimum required thrust, thrust-to-weight ratio, while maintaining a critical system. This ideal space is presented in Figure 6.9. Inside the plotted region are the engine designs that meet the thrust, thrust to weight, and criticality requirements. Further optimization should focus on searching the design region encompassing split ratios 0.35 to 0.45 and ME:FE ratios of 1.30 to 1.35. The highest performing I_{sp} core based on these constraints has an axial split of 0.40, an ME:FE ratio of 1.36. The minimum I_{sp} was barely achieved. The Phoebus 2A design encountered similar radial peaking issues, and used variable uranium enrichment zoning to flatten the radial power distribution with a fixed fuel element moderator element configuration [49].

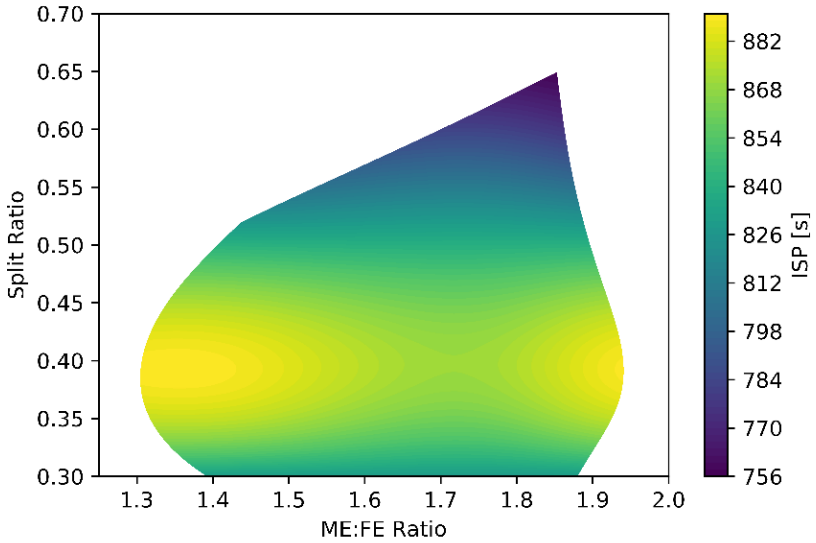

Figure 6.9 Ideal Design Space Map

However, reducing the uranium enrichment in LEU NTPs would result in an increase in the number of moderator elements required to achieve a critical system and decrease the thrust produced by the engine. Instead, the arrangement of the moderator elements in the core could be adjusted to flatten the power profile. Core pattern optimization is outside the scope of this thesis, since optimizing the core pattern should consider the entire mission cycle and not only a single beginning of life point. In order accurately evaluate the performance of a specific core the most limiting operational condition must be used to calculate the core I_{sp}. This analysis should include drum rotation and fuel poisoning effects on the radial and axial power shapes.

Table 6.1 : Ideal core configuration performance

	Unit	**NASA Requirement**	**Core Performance**
I_{SP}	s	875-950	889
Thrust	klb_f	25.00	31
Thrust to Weight	unitless	3.5	4.3
Engine Mass	lb, kg	7143, 3240	7097, 3220
Core Diameter	m	4.6	1

CHAPTER 7 CONCLUSIONS

A summary of the work performed and the conclusions drawn are presented herein. Some additional aspects of work to be further developed are explained.

7.1 Conclusions

The majority of published nuclear thermal propulsion research has focused on HEU fuel designs, which can provide extremely compact and high performing cores. However, the current regulatory environment has restricted NTP designs to use LEU fuels. This restriction forces the increased use of moderator elements in the core to achieve a thermal spectrum. Previous HEU core designs have relied on fixed moderator and fuel element patterns, which are no longer applicable. This thesis explores the effects of perturbing the moderator to fuel element ratio, and the axial split to determine their effects on engine performance and the ability of the engine to meet the NASA DRA 5.0 requirements.

The near-optimal design space presented is the result of numerous neutronic thermal-hydraulic, and system analysis. Full-core neutronic analysis has been conducted using Serpent 2 with coupled gamma transport. Accounting for photon heating effects allows for a more accurate calculation of the axial power profile. Thermal-hydraulic solutions were obtained using a nuclear thermal propulsion specific 1.5-dimensional sub-channel code, NTP-THERMO. Accurate boundary conditions for each thermal hydraulic channel were determined using the POWER system code, which also accounted for heat transfer from the fuel element to the moderator element. The performance of each core configuration was determined via the POWER code iterating on the maximum allowable power while using the centerline fuel temperature, the required pump power to achieve a target chamber pressure, and iterating on the mass flow to achieve a target exit Mach number.

The results obtained in this thesis show that providing accurate power profiles and boundary conditions for each thermal hydraulic channel can have significant impacts on the performance of the engine. Accurately accounting for the fuel inlet conditions and axial power shape is vital to accurately determine a realistic I_{sp} of each engine. The inlet

conditions and axial power shape have a strong influence on the location of the limiting thermal hydraulic node, and the maximum possible reactor power. Higher inlet temperatures allow for better heat transfer in the fuel elements. The assumption of inlet fuel conditions could lead to significant under or over estimations of engine's I_{sp}. The thrust, weight, and thrust to weight ratio are less sensitive to the system boundary conditions, but are still affected since they are dominated by the mass flow rate.

The results in this thesis confirms the feasibility of low enriched fuels and shows that a low enriched engine could achieve the required NASA DRA 5.0 performance requirements and can greatly outperform the theoretical limit for chemical propulsion systems. An optimal design space of split ratios of 0.35 to 0.45 and ME:FE ratios of 1.30 to 1.35 has been identified for further study.

7.2 Future Work

The design of nuclear thermal propulsion engines is a field that has been recently re-vitalized and still has large amount of gaps and unknown questions. As such, there is a large amount of work that needs to be conducted before any system will be flight ready. The work presented in this thesis demonstrates the importance of accounting for full system effects on the design space. Higher fidelity analysis should be applied to the area of interest identified. Additionally, these higher fidelity analyses should account for thermal hydraulic feedbacks on the realistic axial and radial power profiles. The tightly coupled relation between the thermal and neutronic feedback must also be accounted for; the thermal feedback may change the profiles and peaking factors, which in turn could change the thermal properties and thus the location of the limiting node. Capturing the coupled in

nature phenomena will allow to accurately evaluate the maximum achievable I_{sp} of the engine. The Taylor heat transfer correlation should be further investigated to confirm the dependence of the surface to bulk temperature ratio dependence. The correlation was generated for limited operational case (e.g. Reynolds numbers) and specific geometries and thus may be questionable as a general model. A potential remedy is the application of modern computational fluid dynamics codes for extending or modifying the existing correlations.

A more detailed thermal hydraulic solutions should be applied to account for the heat conduction within the moderating element and the heat transfer between the supply and return channels. Accurately accounting for this effect would allow for a more accurate calculation of the maximum temperature in the moderator material and the temperature gradients, which may influence hydrogen disassociation effects in the hydride material. Additionally, this higher fidelity solution will allow for the POWER script to consider the thermal hydraulic limitations of the moderator elements. Consideration of intra-element peaking inside the fuel elements would allow for the calculation of orifficing patterns which will have a strong influence on the pressure drop across the fuel and therefore effect the required pump power, and thus the inlet conditions to the fuel element due to more energy being extracted by the turbine.

REFERENCES

[1] NASA Lewis Research Center, "An Overview of Tested and Analyzed NTP Concepts," *Conference on Advanced Space Initative Technologies*, September, 1991.

[2] Houts M., 2018. Advanced Exploration with Nuclear Thermal Propulison. https://ntrs.nasa.gov/archive/nasa/casi.ntrs.nasa.gov/20180007303.pdf

[3] Argonne National Lab, 166. *Nuclear Rocket Program Terminal Report, ANL-7236*.

[4] J. Witter, 1999. Thermal Hydraulics of Pebble Bed Nuclear Thermal Propulison. Massachusetts Institute of Technology, Docoratal Disseration.

[5] Finseth J. L., 1991. Rover Nuclear Rocket Engine Program: Overivew of Rover Engine Tests: Final Report. Tech, Rep. NASA-CR-184270

[6] Walton T., 1992. Program ELM: A Tool for Rapid Analysis of Solid-Core Nuclear Rocket Fuel Elements. Lewis Research Center. NASA-TM-105867.

[7] Venneri, P., Kim, Y., 2013. Feasibility of low enriched uranium fuel for space nuclear propulsion. Transactions of the Korean Nuclear Society Spring Meeting 2013. Korean Advanced Institute for Science and Technology.

[8] Messick, C., Galan, J., 2013. Global Threat Reduction Initiative. National Nuclear Security Administration.

[9] Eades M., et al, 2015. SCCTE: An LEU NTP Concept with Tungsten Cermet Fuel. ANS Winter Meeting and Nuclear Technology Expo

[10] Krecicki M., Kotlyar D. Sensitivity Studies of the Tungsten Vector on the Performance of a LEU NTP Engine, Nuclear and Emerging Technologies for Space, Richland, WA, 2019.

[11] NASA, Space Technology Mission Directorate Game Changing Development Program, FY19 Annual Review https://ntrs.nasa.gov/archive/nasa/casi.ntrs.nasa.gov/20190031810.pdf

[12] NASA, 2019. Nuclear Thermal Propulsion Facts Sheet, Marshall Space Flight Center https://gameon.nasa.gov/gcd/files/2018/02/FS_NTP_180213.pdf

[13] NASA, 2019. Nuclear Thermal Propulsion Update https://ntrs.nasa.gov/archive/nasa/casi.ntrs.nasa.gov/20190004963.pdf

[14] Emrich W., 2017. Nuclear Cryogenic Propulsion Stage (NCPS) Fuel Element Testing in the Nuclear Thermal Rocket Element Environmental Simulator (NTREES). NASA.

[15] Drake B.G. et al., 2009a. Human Exploration of Mars: Design Reference Architecture 5.0. Tech. Rep. NASA/SP-2009-566.

[16] Husemeyer, P.J.A., 2016. Design and Optimization of a Low-Enriched Uranium Nuclear Thermal Rocket Engine. University of Cambridge Doctoral thesis.

[17] Lewis, J.V., 1967. Estimating Thermal Conductivity of Cermet Fuel Materials for Nuclear Reactor Application. Lewis Research Center, Cleveland, Ohio Tech. Rep. NASA TN D-3898.

[18] Lassner, E., Schubert, W.D., 2012. Tungsten: Properties, Chemistry, Technology of the Elements, Alloys, and Chemical Compounds. Springer.

[19] Brookhaven National Laboratory, National Nuclear Data Center, Sigma. https://www.nndc.bnl.gov/sigma/.

[20] Lundberg L., 1981. A Critical Evaluation of Molybdenum and Its Alloys for Use in Space Reactor Core Heat Pipes. Los Alamos National Lab, LA-8685-MS.

[21] Takkunen P., 1969. Uranium Nitride and Tungsten or Molybdenum from Mixed Powders and From Coated Particles. Lewis Research Center. NASA TN D-5136.

[22] Sterbentz J., 2018. Preliminary Assessment of Two Alternative Core Design Concepts for the Special Purpose Reactor. Idaho National Laboratory.

[23] Webb J., Charit I, 2012. Analytical determination of thermal conductivity of W–UO2 and W–UN CERMET nuclear fuels. Journal of Nuclear Materials. 427 87–94.

[24] Benensky k. et al., 2019. Recent FY18/FY19 NTP Materials Development Activities at NASA Marshal Space Flight Center, Nuclear and Emerging Technologies for Space, Richland, WA, 2019.

[25] NASA SBIR 2019 Phase I Solicitation. https://sbir.nasa.gov/content/nuclear-thermal-propulsion-ntp-0

[26] Stewart M., 2019. Thermal, Fluid, and Neutronic Analysis of an LEU Nuclear Thermal Propulsion Core. VPL at NASA Glenn Research Center. AIAA Propulsion and Energy 2019 Forum.

[27] Simnad, M.T., 1981. The U-ZrHx Alloy: its properties and use in TRIGA Fuel. Nucl. Eng. Des. 64 (3), 403–422.

[28] Houten R., Baxter W., "Titanium, zirconium, and yttrium hydrides as space shielding materials." Journal of Spacecraft and Rockets, 2.3, 469-472 (1965).

[29] Coleman T.L. et al., 1970. Nuclear and Space Radiation Effects on Materials. Tech. Rep. NASA/SP-8053.

[30] Westinghouse Astro Nuclear Laboratory, 1970. Bath Shield Material Development Test Report. WANL-TME-2737.

[31] Belair M. et al., 2013. Nuclear Thermal Rocket Simulation in NPSS. NASA Glenn Research Center.

[32] Leppänen, J., Pusa, M., Viitanen, T., Valtavirta, V., Kaltiaisenaho, T., 2015. The Serpent Monte Carlo code: Status, development and applications in 2013. Ann. Nucl. Energy 82, 142–150.

[33] Leppänen, J., Mattila, R., Pusa, M., 2014. Validation of the Serpent-ARES code sequence using the MIT BEAVRS benchmark – initial core at HZP conditions. Ann. Nucl. Energy 69, 212–225.

[34] Ikonen, T., Loukusa, H., Syrjälahti, E., Valtavirta, V., Leppänen, J., Tulkki, V., 2015. Module for thermomechanical modeling of LWR fuel in multiphysics simulations.

[35] Leppänen, J., 2010. Performance of Woodcock delta-tracking in lattice physics applications using the Serpent Monte Carlo reactor physics burnup calculation code. Ann. Nucl. Energy 37, 715–722.

[36] D. A. Brown et al., "ENDF/B-VIII.0: The 8th Major Release of the Nuclear Reaction Data Library with CIELO-project Cross Sections, New Standards and Thermal Scattering Data," Nucl. Data Sheets, vol. 148, pp. 1–142, 2018.

[37] Leppänen, J., et al, 2017. Development of a Coupled Neutron / Photon Transport Mode in the Serpent 2 Monte Carlo Code. International Conference on Mathematics & Computational Methods Applied to Nuclear Science & Engineering.

[38] J. Holman, Heat Transfer, McGraw-Hill Book Company (1986)

[39] Busard, DeLaur, 1958. Nuclear Rocket Propulsion. McGraw-Hill.

[40] Lewis, J.V., 1967. Estimating Thermal Conductivity of Cermet Fuel Materials for Nuclear Reactor Application. Lewis Research Center, Cleveland, Ohio Tech. Rep. NASA TN D-3898.

[41] Lundberg L., 1981. A Critical Evaluation of Molybdenum and Its Alloys for Use in Space Reactor Core Heat Pipes. Los Alamos National Lab, LA-8685-MS.

[42] Webb J., Charit I, 2012. Analytical determination of thermal conductivity of W–UO2 and W–UN CERMET nuclear fuels. Journal of Nuclear Materials. 427 87–94.

[43] Miller J., 1967. Estimating Thermal Conductivity of Cermet Fuel Materials for Nuclear Reactor Applications. NASA-TN-D3898.

[44] Bruggeman, D.A.G., 1935. Berechnung Verschiedener Physikalischer Konstanten von Heterogenen Substanzen. Annalen der Physik (Leipzig) 24, 636–679.

[45] IAEA, 2006. Thermophysical properties database of materials for light water reactors and heavy water reactors. Tech. Rep. IAEA-TECDOC-1496.

[46] Matsuo, H., 2000. Measurements of thermal diffusivities of fine-grained isotropic graphites from room temperature to 2000 °Cy laser flash method. Netsu Sokutei 17 (1), 2–8.

[47] Sutton, G.P., Biblarz, O., 2001. Rocket Propulsion Elements, 7th edition. John Wiley & Sons.

[48] Gates J., Kotlyar D., et al, 2018. Low-enriched cermet-based fuel options for a nuclear thermal propulsion engine. Nuclear Engineering and Design 331 313-330.

[49] Sapir J., Orndoff J., 1973. Neutronics of Pheobus-2A Reactor. Los Alamos Scientific Laboratory of the University of California.